

Tailored plasmon polariton landscape in graphene/boron nitride patterned heterostructures

Golenić, Neven; de Gironcoli, Stefano; Despoja, Vito

Source / Izvornik: **npj 2D Materials and Applications**, 2024, 8

Journal article, Published version

Rad u časopisu, Objavljena verzija rada (izdavačev PDF)

<https://doi.org/10.1038/s41699-024-00469-6>

Permanent link / Trajna poveznica: <https://urn.nsk.hr/urn:nbn:hr:217:020228>

Rights / Prava: [Attribution 4.0 International](#)/[Imenovanje 4.0 međunarodna](#)

Download date / Datum preuzimanja: **2025-01-11**



Repository / Repozitorij:

[Repository of the Faculty of Science - University of Zagreb](#)



<https://doi.org/10.1038/s41699-024-00469-6>

Tailored plasmon polariton landscape in graphene/boron nitride patterned heterostructures

Check for updates

Neven Golenić ^{1,2} ✉, Stefano de Gironcoli ^{1,3} & Vito Despoja ^{4,5}

Surface plasmon polaritons (SPPs), which are electromagnetic modes representing collective oscillations of charge density coupled with photons, have been extensively studied in graphene. This has provided a solid foundation for understanding SPPs in 2D materials. However, the emergence of wafer-transfer techniques has led to the creation of various quasi-2D van der Waals heterostructures, highlighting certain gaps in our understanding of their optical properties in relation to SPPs. To address this, we analyzed electromagnetic modes in graphene/hexagonal-boron-nitride/graphene heterostructures on a dielectric Al_2O_3 substrate using the full ab initio RPA optical conductivity tensor. Our theoretical model was validated through comparison with recent experiments measuring evanescent in-phase Dirac and out-of-phase acoustic SPP branches. Furthermore, we investigate how the number of plasmon branches and their dispersion are sensitive to variables such as layer count and charge doping. Notably, we demonstrate that patterning of the topmost graphene into nanoribbons provides efficient Umklapp scattering of the bottommost Dirac plasmon polariton (DP) into the radiative region, resulting in the conversion of the DP into a robust infrared-active plasmon. Additionally, we show that the optical activity of the DP and its hybridization with inherent plasmon resonances in graphene nanoribbons are highly sensitive to the doping of both the topmost and bottommost graphene layers. By elucidating these optical characteristics, we aspire to catalyze further advancements and create new opportunities for innovative applications in photonics and optoelectronic integration.

One of the many properties of graphene, with possible applications in optoelectronics, biosensing, photovoltaics, etc., is its ability to support surface plasmon polariton modes (SPPs); the electromagnetic (EM) modes in which the photon strongly hybridises with electronic density oscillations^{1–8}. The SPP electrical field is localised in the perpendicular z direction and thus propagates along the xy plane. Considering that in graphene, SPPs exhibit low damping⁴, these plasmonic modes possess extended lifetimes, low losses and long propagation lengths^{2,9–13}.

Pristine graphene supports a broad π plasmon in the ultraviolet (UV) frequency range. However, once the graphene is carrier-doped (either by holes or electrons), the low-lying intraband $\pi \rightarrow \pi$ electron–hole excitations (in the vicinity of the K point) and photons become entangled which initiates the formation of collective photon-polarisation modes called

plasmon polaritons, also known as Dirac plasmon polaritons (DP). DP is a p(TM) polarised EM mode producing a longitudinal electrical field which oscillates parallel to the direction of propagation \mathbf{Q} , i.e. along the graphene sheet. In the optical limit ($Q \approx 0$) it has a linear dispersion (Qc), which, in the short wavelength limit, $Q \sim 1/a$ (where a is the unit cell length), converts into a square-root dispersion, $\sim \sqrt{Q}$ ¹⁴. For each additional graphene layer introduced, another in-plane mode appears and hybridises with the already existing ones forming plasmon polariton mode known as the acoustic plasmon (AP) due to its linear-like dispersion ($v_F Q$). The AP produces an in-plane electrical field directed oppositely in each distinct layer, i.e. the electrical fields in two layers oscillate out-of-phase. By further stacking differently doped graphene layers one can achieve van der Waals heterostructures (vdW) with diverse plasmonic properties^{7,15}. Unfortunately, due to strong

¹Scuola Internazionale Superiore di Studi Avanzati, Via Bonomea 265, I-34136 Trieste, Italy. ²Department of Physics, University of Zagreb, Bijenička 32, HR-10000 Zagreb, Croatia. ³CNR-IOM DEMOCRITOS, Istituto Officina dei Materiali, Trieste, Italy. ⁴Institute of Physics, Bijenička 46, 10000 Zagreb, Croatia. ⁵Donostia International Physics Center (DIPC), P. Manuel de Lardizabal, 4, 20018 San Sebastián, Spain. ✉e-mail: ngolenic@sissa.it

charge density overlap between two adjacent layers and consequently strong screening, these plasmon modes are suppressed, and hence graphene alone fails to fulfil the promise of a wonder material in this regard. Fortunately, the advent of on-demand manufacturing of vdW, which are weakly bound quasi-2D crystals composed of many monolayers stacked in a precise sequence¹⁶, has made it possible to overcome this issue. Hence, instead of building a graphene bilayer, another layer can be inserted in-between where the new layer is carefully selected to be weakly polarisable and transparent in the frequency range of SPPs. In other words, the in-between layers should have no possible electronic excitations in the energy range of graphene interband $\pi \rightarrow \pi^*$ transitions. An ideal candidate is hexagonal boron nitride (*h*-BN) which is a large-bandgap semiconductor^{17,18}. The existence of both Dirac and acoustic SPPs in bilayer graphene was already predicted using the finite-difference frequency-domain method¹⁹. However, the applied method made use of the frequency-independent surface conductivity and graphene layers were considered as dielectric slabs of finite thickness while being kept artificially spaced apart without an explicit insulating spacer layer in between. The potential for vdW heterostructures to exhibit exotic plasmonic properties arises in alternating layers of conductive and semi-conductive 2D crystals. These structures can host multiple plasmonic branches spanning a broad IR frequency range, and hold the possibility of targeted optical activation. If such a heterostructure is periodic then a plasmonic band structure can form in the direction perpendicular to the crystal, in analogy with photonic bands in Bragg crystals²⁰. The promise of van der Waals heterostructures is evident in the huge effort by the experimental community which has led to several successful synthesis alleys for graphene/*h*-BN composites, most notably using exfoliation, chemical vapour decomposition and epitaxial growth^{16,21–26}. Only recently, experimental efforts²⁷ have been made to identify vertical interlayer plasmon-plasmon coupling (and thus the formation of DP and AP modes) in a GR/*h*-BN/GR trilayer supported on a SiO₂ substrate with the help of near-field infrared nano-imaging technique. Hu et al.²⁷ have also investigated the effect of increasing the number of *h*-BN layers to explore how the coupling between plasmons in the two graphene layers decays as the separation between them increases. The latter motivated us to choose this very system as the benchmark for the ab initio theoretical approach presented in this paper; the only difference being our choice of substrate where Al₂O₃ was chosen instead of SiO₂. We also further extended our modelling to explore the multiplication of plasmon branches in alternating GR/*h*-BN/GR/*h*-BN/... thin films on an Al₂O₃ substrate.

Another challenge in observing exotic plasmonic modes is their evanescent character, making it hard to directly excite them through light. However, an alternative approach is to excite them indirectly over the sub-wavelength tip of a scattering-type scanning near-field optical microscope (s-SNOM)¹, or by patterning the topmost graphene layer into nanoribbons^{4,28–33}, and adopting it as an atomic-scale grating. Another advantage of graphene nanoribbons (GNR) is that their optical response can be tuned in the terahertz region by applying an external magnetic field²⁹. Although beyond the scope of this study, this opens another avenue in the quest to unlock nanoscale applications for graphene vdW heterostructures by fine-tuning and enhancing their response properties.

To calculate the electromagnetic response in vdW heterostructures, we adapted two ab initio models: (1) a fully atomistic model which can be applied to vdW heterostructure consisting of several stacked 2D layers (eg. GR/*h*-BN/GR heterostructure) and (2) a 2D model which is analogous to the atomistic model though the interlayer orbital hybridisation and crystal local field effects are neglected. The latter can be applied to vdW heterostructures consisting of an arbitrary number of 2D layers. Due to the lack of computationally cheap theoretical descriptions of optical properties from first principles, most experimental groups apply a finite difference method (FDM)^{19,34–36}, which uses the local frequency-dependent optical conductivity $\sigma(\omega)$. Moreover, if 2D ab initio conductivities $\sigma^i(\omega)$ (for each layer *i* in the composite) were used, the accuracy of the FDM would likely, in terms of accuracy, be on par with the 2D method presented in this work. However, if the FDM model treats the entire composite as a single dielectric slab

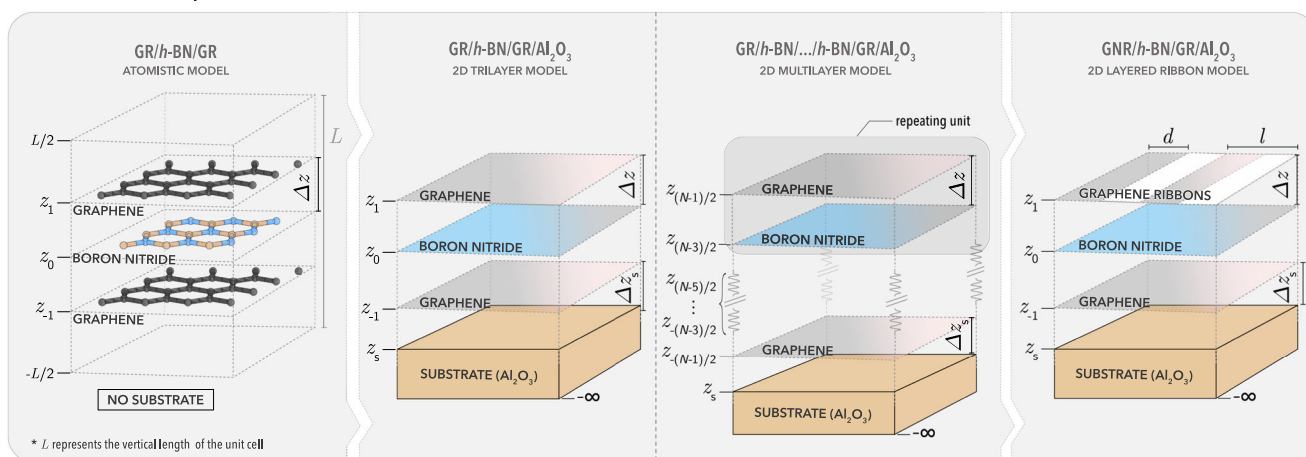
described by an averaged local conductivity (or e.g. a macroscopic dielectric function), or in the best case scenario, as stacked layers of finite thicknesses (each one described by a local macroscopic dielectric function $\epsilon^i(\omega)$)¹⁹, it will fail to properly describe the properties of both the DP and APs. Another theoretical formulation of the dielectric response in multilayer vdW heterostructures was proposed in ref. 37; however, their model completely neglects photon retardation effects. Given that our 2D model is derived from approximations on a fully atomistic description and includes retardation effects, it naturally overcome this issue.

In our fully atomistic model, the current fluctuations in the entire vdW heterostructure are described by nonlocal conductivity tensor (σ), which is equivalent to the photon self-energy, and the unscreened electron–electron or current–current interactions are mediated by the free electrical field propagator (Γ^0)^{14,38}. By solving Dyson's equation in the random phase approximation (RPA) we obtain the screened electrical field propagator (\mathcal{E}) whose negative real part represents the spectrum of electromagnetic modes ($S = -\text{Re } \mathcal{E}$). Calculating these spectra for different 2D transfer wavevectors gives us the dispersion relations of both collective and single-particle electromagnetic modes.

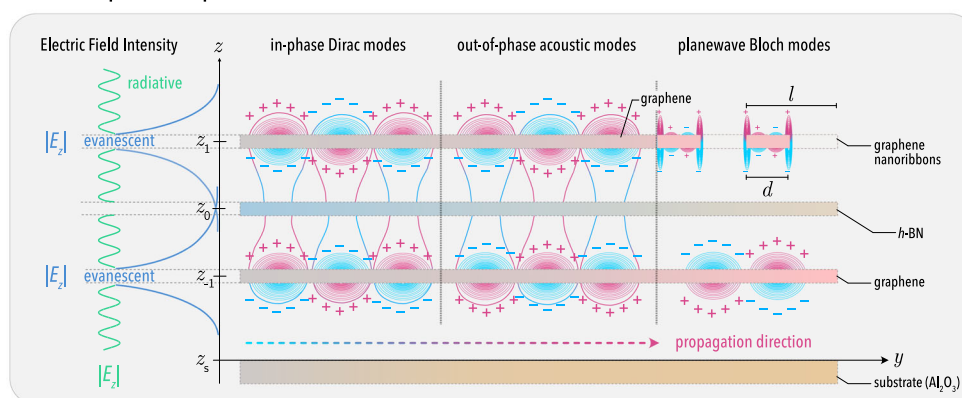
The 2D model introduced here represents an extension to the atomistic model developed in ref. 14 to simulate the conductivity or current–current nonlocal tensor in very large vdW heterostructures, including dielectric substrates while still keeping very good agreement with the atomistic model. In the 2D model, the partial *nonlocal* conductivity tensors in each 2D layer (here GR and *h*-BN) are first calculated separately. Then the total nonlocal conductivity of the vdW composite is obtained by performing a summation over partial conductivity tensors centred around the equilibrium positions (along the *z*-axis) of the corresponding 2D layer in the vdW composite. In the first panel of Fig. 1a, we show the reference structure of the GR/*h*-BN/GR van der Waals crystal as described in the atomistic model, where crystal local field effects are included. The variable z_i represents the position of each layer along the perpendicular crystal cell axis, where z_0 is chosen as the origin when computing the electrical field propagator. If the crystal local field effects are also excluded ($\mathbf{G} = \mathbf{G}' = \mathbf{0}$ in the partial conductivity tensors) this modelling becomes equivalent to the inherently 2D model where layers are essentially 2D sheets distributed at equilibrium positions and described by local 2D conductivities $\sigma(\omega)$. In the optical limit this procedure works perfectly well, allowing us to investigate very large heterostructures (see 3rd panel of Fig. 1a) and at the same time, tremendously cutting down on computational time. Equally important is the addition of a substrate to realistically depict an experimental setup, which our 2D model easily addresses. Namely, the electromagnetic field scattering at the dielectric substrate (here Al₂O₃) can be easily turned on by modifying the free electric field propagator $\Gamma^0 \rightarrow \Gamma^0 + \Gamma^{\text{sc}}$, where the scattered field Γ^{sc} is derived by solving Maxwell's equations with the appropriate boundary conditions. In comparison, introducing a substrate in the full atomistic model would require adding at least five atomic layers of the desired substrate material to the crystal structure, which would make solving Dyson's equation for the electric field propagator prohibitively expensive to compute.

It's important to highlight that 2D modelling is accurate only in the optical or long-wavelength limit. Specifically, this holds true when the wavelength λ is significantly larger than the dimensions of the parallel or perpendicular unit cells *a* and *L*, respectively, in a single 2D layer (GR or *h*-BN). Moreover, the 2D model accurately describes plasmonic properties in the metallic subsystem (here GR); however, it is unable to fully reproduce the electromagnetic response in the semiconductive subsystem (here *h*-BN). Further improvement could be achieved by renormalising the semi-conductive bandgap within the GW approximation as well as adding vertex corrections to correctly describe electron–hole binding (excitonic effects). Nevertheless, these effects negligibly influence the plasmonic excitations in the IR frequency range ($\omega < 1$ eV) studied here. Instead, they mostly influence the UV region (4–7 eV), in particular, the $\pi \rightarrow \pi^*$ electronic excitations at M and K points in GR and *h*-BN layers, respectively. Finally, we also neglected electron–phonon interactions which might play an important role in the IR region (<200 meV), where the hyperbolic phonon-

a Structure & Composition



b Surface plasmon polaritons



c Electron excitations

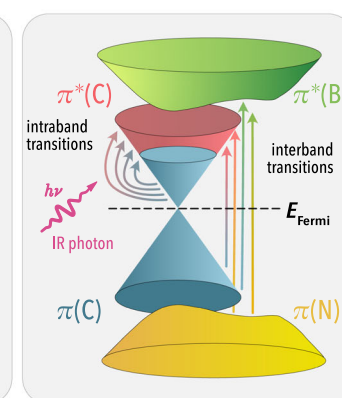


Fig. 1 | Electromagnetic modes in multilayer geometries of GR/h-BN. Schematic representation of a heterostructure composition and geometry depicted in the atomistic model and in the 2D approximation where each layer is collapsed into conductive sheets which also include substrate polarisation effects. The variable z_i represents the vertical position of each layer, where $z_0 = 0$ is the origin. **b** Electric field of a surface plasmon polariton wave propagating along the \hat{y} direction. The electrical field ($|E_z|$) of the evanescent EM modes decay exponentially in the vacuum

region (depicted in blue). When the top layer is replaced by nanoribbons, additional radiative modes appear, exhibiting an oscillatory field intensity (depicted in green). **c** Single-particle interband and plasmonic intraband electronic excitations between bands near the K high-symmetry point. The inner conus represents graphene valence $\pi(C)$ and doped conduction $\pi^*(C)$ bands, while the outer bands correspond to nitrogen $\pi(N)$ and boron $\pi^*(B)$ bands which contribute only to interband transitions.

polaritons of $h\text{-BN}^{17,39-42}$ could possibly interact with plasmon polaritons in GR layers.

In this paper, we first explore the electromagnetic modes in GR/h-BN/GR for differently electron-doped graphene $n = 0 \text{ e cm}^{-2}$, $1 \times 10^{13} \text{ e cm}^{-2}$, $5 \times 10^{13} \text{ e cm}^{-2}$ and $1 \times 10^{14} \text{ e cm}^{-2}$ whose nonlocal conductivity tensor is calculated from first principles using two complementary models; a slow but highly accurate atomistic model, and a faster and more versatile 2D model. After validating the 2D model, we explore the multifaceted tuning of the intensities and dispersion relation of infrared DP modes by varying the number of layers in GR/h-BN/... van der Waals heterostructures, as well as surface charge carrier doping. By patterning the topmost GR layer into GNRs, we shed light on understanding the interplay between plasmon resonances (optically active plasmons supported by self-standing GNRs), Bloch DP (Bragg scattered Dirac plasmon polariton in bottom graphene) in differently doped GNR and the bottom graphene layer.

In the following paragraph, we briefly introduce the geometry of the studied systems. The atomistic model system consists of two GR layers centred at vertical positions z_1 and z_{-1} and a $h\text{-BN}$ layer at the origin $z_0 = 0$ of the unit cell, as shown in the first panel of Fig. 1a. The GR \leftrightarrow $h\text{-BN}$ separation is denoted by Δz , and the unit cell in the z direction by L .

In the 2D model for the trilayer GR/h-BN/GR/ Al_2O_3 , GR and $h\text{-BN}$ sheets are placed at equivalent positions and the dielectric substrate is

introduced below the bottom graphene layer at a position z_s , as shown in the 2nd panel of Fig. 1a. The substrate occupies the semi-infinite $[z_s, -\infty)$ half-space, and the separation between the substrate and bottom graphene is denoted with Δz_s . In this case the system is no longer bounded by a crystal unit-cell.

The 2D model allows us to study more complex heterostructures with an arbitrary number of layers N , thus the trilayer geometry can be generalised to a multilayered heterostructure consisting of periodic repetitions of GR/h-BN subunits, as illustrated in the 3rd panel of Fig. 1a. In this case GR sheets occupy the $z_i = z_{\pm 1}, z_{\pm 3}, \dots, z_{\pm(N-1)/2}$ planes where i are odd integers while $h\text{-BN}$ sheets occupy $z_i = z_0, z_{\pm 2}, \dots, z_{\pm(N-3)/2}$ planes where i are even integers. The origin of the system is always placed in the plane of the central $h\text{-BN}$ layer ($z_0 = 0$) for convenience, while the surface (top) of the dielectric substrate is placed in the $z_s = z_0 - \frac{N-1}{2} \Delta z - \Delta z_s$ plane (i.e. below the bottom GR layer $z_s < z_{-(N+1)/2} \ll z_0 = 0$) and extends below to cover the semi-infinite $[z_s, -\infty)$ half-space. The distance parameters Δz and Δz_s are considered fixed, as in the case of the GR/h-BN/GR heterostructure.

Finally, we shall also investigate the electromagnetic modes in the GNR/h-BN/GR/ Al_2O_3 composite which is in fact a GR/h-BN/GR composite where the topmost (GR) layer at position z_1 is patterned into nanoribbons (GNR) of width d and period l , also including the substrate, as illustrated in the last panel of Fig. 1a Here we suppose that the substrate

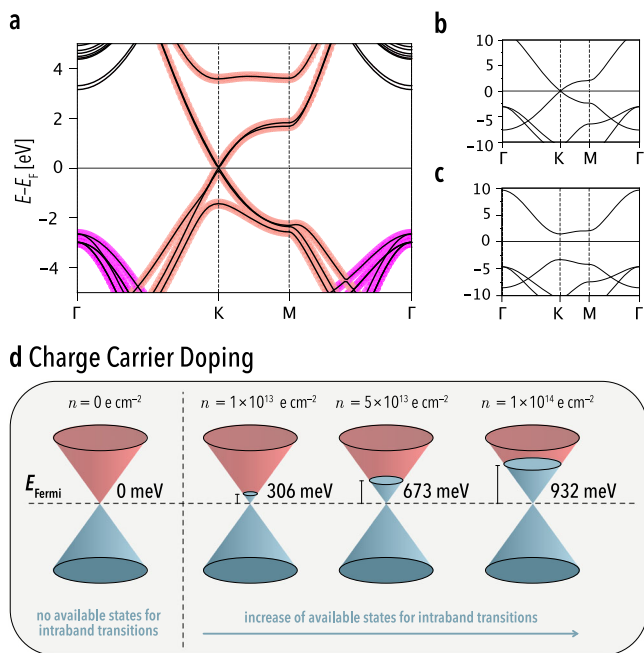


Fig. 2 | Band symmetry and charge carrier doping. Band structures of the **a** GR/*h*-BN/GR trilayer and self-standing **b** GR and **c** *h*-BN single-layers. Magenta and red colouring of bands indicate their respective σ (denoted in magenta) and π (denoted in red) symmetry character as obtained by projecting the band structure onto atomic states. **d** Schematic close-up of the band structure near the K high-symmetry point illustrating the levels of electrostatic doping and corresponding Fermi energy shifts in GR/*h*-BN/GR.

polarisation is described by the local dielectric function $\epsilon_z(\omega)$, while the polarisation of the dielectric media occupying the region $z > z_s$ is described by the dielectric constant ϵ_0 .

In Fig. 1b, we draw a scheme of the asymmetric AP and symmetric DP modes of graphene propagating along the y -axis while on the left-hand side we illustrate the spatial confinement of the modes by plotting the evanescent electrical field $|E_z|$ (indicated in blue) which can be seen as quickly decaying away from the graphene layers. In contrast, once the topmost layer is patterned into graphene nanoribbons, additional modes appear inside and at the ribbon edges. These modes can have both evanescent and radiative character ($|E_z|$ indicated in green). Due to its large band-gap the *h*-BN spacer will only slightly be polarised (by the evanescent SPP field) and will thus have a negligible effect on the induced fields.

In Fig. 1c, we illustrate the possible electronic excitations between graphene valence $\pi(C)$ (subvalence $\pi(N)$ localised on nitrogen atoms) and graphene conduction $\pi^*(C)$ ($\pi^*(B)$ localised on boron atoms) bands in the GR/*h*-BN/GR trilayer. Interband excitations involve direct electron transitions between different energy bands, while intraband excitations occur within the same (in this case $\pi^*(C)$ band of surface charge carrier doped graphene). The latter can couple with infrared (IR) photons (usually coinciding with a change in momentum) to form SPPs^{2,14,22}.

Results

Ground state electronic structure

We begin our discussion by comparing the band structure of GR/*h*-BN/GR (Fig. 2a) and its individual graphene (Fig. 2b) and *h*-BN (Fig. 2c) layers. By examining the trilayer band structure we can deduce it contains a blend of unperturbed bands from its monolayer components, almost without any hybridisation. The only difference being in the splitting of the two graphene π, π^* bands and the opening of a tiny gap (<5 meV) at the K high-symmetry point due to weak degeneracy breaking. We can thus infer that the overlap

between the electron charge densities of particular layers of graphene and *h*-BN is negligible.

Consequently, this implies that the nonlocal optical conductivities of the individual 2D layers are weakly affected by being stacked in a heterostructure, so that the electrodynamical response of the entire vdW heterostructure can be calculated by implementing a 2D model, i.e. by combining the electrodynamical responses of individual monolayers calculated within the atomistic model (as described in “Theoretical Formulation”).

In order to observe SPP modes, which are due to intraband $\pi \rightarrow \pi$ (or $\pi^* \rightarrow \pi^*$) transitions near the K point, the trilayer was electron-doped (Fig. 2d) which also had no observable effect on the band structure other than shifting up the Fermi level with increasing doping. Hence, the Fermi energy of the two graphene layers increases from 0 meV to 306 meV and 673 meV up to 932 meV, for the four doping carrier densities applied; $n = 0 \text{ e cm}^{-2}$, $n = 1 \times 10^{13} \text{ e cm}^{-2}$, $n = 5 \times 10^{13} \text{ e cm}^{-2}$ and up to $n = 1 \times 10^{14} \text{ e cm}^{-2}$, respectively.

Similarly, for the 2D model, monolayers of graphene were doped by half the values of surface carrier density in the trilayer to reproduce the same level of doping. Given that freestanding *h*-BN has a large bandgap, the doping charge only fills graphene bands. Consequently, there is no interference between the Dirac plasmon (which is expected to appear below 1.5 eV) and *h*-BN interband electron-hole excitations, thus confirming *h*-BN is an ideal spacer for graphene plasmonics.

Surface plasmon polaritons

In order to better understand the properties of 2D plasmons appearing in the GR/*h*-BN/GR heterostructure it can be useful to analyse a more phenomenological toy model where the polarisability due to interband excitations ($\sigma^{\text{inter}} = 0$) is neglected. This completely excludes the influence of *h*-BN, and the polarisability of graphene is reduced only to the intraband conductivity (Eq. (21)). Moreover, because graphene is isotropic and non-conductive in the vertical z direction the effective numbers of charge carriers are $n_x = n_y$ and $n_z = 0$. According to these conditions, the p(TM) component of Dyson’s equation (eq. (25)) becomes $\hat{\epsilon}_p \mathcal{E}_p = \Gamma_p$, where we have defined the p(TM) or longitudinal dielectric tensor, in the evanescent region $\omega < Qc$, as

$$\hat{\epsilon}_p(Q, \omega) = \mathbb{I} - \tilde{\beta}_0 \frac{\omega_p^2}{\omega^2} \begin{bmatrix} 1 & e^{-2\tilde{\beta}_0 \Delta z} \\ e^{-2\tilde{\beta}_0 \Delta z} & 1 \end{bmatrix}, \quad (1)$$

where $\tilde{\beta}_0 = \sqrt{Q^2 - \frac{\omega^2}{c^2}}$ and $\omega_p = \sqrt{\frac{2\pi n_s e^2}{m}}$. Above, we also used the definition of the bare propagator (Eq. (26)), where $\Gamma^\infty = 0$. By solving the eigenvalue problem $\hat{\epsilon}_p \mathbf{E}_p = 0$ we obtain two plasmon modes, whose dispersion relations (in the non-retarded limit, $c \rightarrow \infty$) are

$$\omega_\pm(Q) = \omega_0(Q) \sqrt{1 \pm e^{-2Q\Delta z}}. \quad (2)$$

These two plasmon modes produce an electrical field which in the neighbouring graphene layers oscillates in-phase $\mathbf{E}_p^+ = (1, 1)$ and out-of-phase $\mathbf{E}_p^- = (1, -1)$. Because in the longwavelength limit ($Q \rightarrow 0$) one obtains $\omega_+(Q) \approx \omega_p \sqrt{2Q}$ and $\omega_-(Q) \approx \omega_p \sqrt{2\Delta z Q}$; plasmon ω_+ (due to its square-root dependence) is denoted as DP and plasmon ω_- (due to its linear dependence) is referred to as AP⁴³.

In Fig. 3, the spectra (Eq. (16)) of p(TM) electromagnetic modes in the GR/*h*-BN/GR trilayer for the three distinct transfer wavevectors (a) $Q = 0.001 a_0^{-1}$, (b) $Q = 0.01 a_0^{-1}$ and (c) $Q = 0.05 a_0^{-1}$ are shown for four different doping concentrations (as noted in Fig. 2d). The spectra were calculated using both models; the atomistic (dotted line) and 2D model (full line). Comparing the two models is essential to

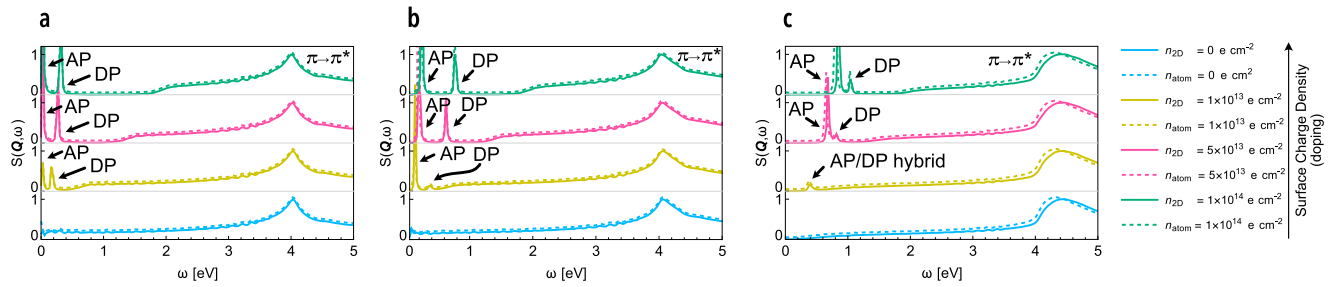


Fig. 3 | Excitation spectra dependence on transfer momentum at different levels of doping. Intensities of p(TM) electromagnetic modes for wave vectors: **a** $Q = 0.001 a_0^{-1}$, **b** $Q = 0.01 a_0^{-1}$, **c** $Q = 0.05 a_0^{-1}$ calculated in the atomistic (dotted line) and 2D model (full line). Colours (blue, yellow, magenta and green)

correspond to increasing levels of surface charge doping ($n = 0 \text{ e cm}^{-2}$, $1 \times 10^{13} \text{ e cm}^{-2}$, $5 \times 10^{13} \text{ e cm}^{-2}$, and $1 \times 10^{14} \text{ e cm}^{-2}$) which increases the intensity and separation of DP and AP electromagnetic modes. Intensities were normalised to unity w.r.t. the $\pi \rightarrow \pi^*$ peak.

explore the validity of approximations applied in the 2D model. As can be seen in all three plots, the spectral shape and peak positions are in a very good quantitative agreement between the two models. In the long wavelength limit $Q = 0.001 a_0^{-1}$ (Fig. 3a), as expected the agreement between the two models is excellent. For the 0-th doping (blue lines) the only contribution comes from the continuum of single particle $\pi \rightarrow \pi^*$ interband transitions which reach a peak in the UV region at 4.2 eV, in both the atomistic and 2D model, corresponding to the Van Hove singularity in graphene. Once doping is introduced (in increasing order depicted by yellow, pink and green lines in Fig. 3), the intraband $\pi^* \rightarrow \pi^*$ channel is open and the AP (lower peak) and DP (upper peak) modes begin to emerge in the IR frequency range. We can observe perfect agreement between plasmon peaks in both models. Moreover, these plasmon peaks agree perfectly with the results obtained in the simple toy model. The effective charge carrier concentrations corresponding to the three doping levels are $n_x = 0.0037 a_0^{-2}$, $0.0081 a_0^{-2}$ and $0.011 a_0^{-2}$, and according to Eq. (2), they correspond to AP/DP plasmon frequencies of $\omega_{-/+}^{\text{toy}} = 14/185 \text{ meV}$, $21/274 \text{ meV}$ and $25/320 \text{ meV}$, respectively. These frequencies are in almost excellent agreement with peaks derived in the atomistic (as well as in the 2D) model $\omega_{-/+}^{\text{at}} = 14/162 \text{ meV}$, $20/267 \text{ meV}$ and $25/319 \text{ meV}$, respectively. Therefore, in the optical limit the AP and DP behave exactly as two coupled hydrodynamic plasmons in two conductive sheets⁴⁴. This supports the presumption about the weak vdW bonding of graphene layers (the existence of two spatially separated 2D plasmons), as well as the weak influence of *h*-BN screening on graphene plasmonics.

Furthermore, by applying the same set of parameters (37 *h*-BN layers sandwiched between two GR sheets doped at $n = 1 \times 10^{13} \text{ e/a}_0^2$ and corresponding to a slab thickness of 12.7 nm) as in ref. 27, the AP and DP peaks obtained experimentally are in excellent agreement with our models.

For the wave vectors beyond the optical limit $Q = 0.01 a_0^{-1}$ (Fig. 3b) and $Q = 0.05 a_0^{-1}$ (Fig. 3c), the agreement between the spectra of the atomistic and 2D models remains very good. This is, to some extent, the expected result considering that the wavelength $\lambda \sim 1/Q$ is still greater than the atomic thickness of the 2D crystal. We only notice that in the 2D model the AP becomes slightly blue-shifted compared to the atomistic one. In contrast, for such large wave vectors the toy model can no longer adequately describe plasmonic modes. For example; for $Q = 0.05 a_0^{-1}$ and the largest effective charge carrier concentration $n_x = 0.011 a_0^{-2}$ one obtains $\omega_{-/+}^{\text{toy}} = 1.24/2.26 \text{ eV}$ while the result of the atomistic model is $\omega_{-/+}^{\text{at}} = 0.813/1.03 \text{ eV}$. As expected, the toy model which omits interband transitions that push plasmons towards lower energies, significantly overestimate atomistic plasmon frequencies. In spite of this shortcoming, the toy model still predicts the presence of out-of-phase modes and offers very accurate estimations of DP and AP energies in the optical limit. In practice, experimental imaging techniques such as electron energy loss spectroscopy,

s-SNOM and similar^{1,4,30}, measure the spectra at and above the top layer breaking the parity symmetry and thus enable the observation of the AP. Equations (16), (17), (27) which represent the intensity of the induced electrical field driven by external oscillating dipole (for example simulating a atomic force microscope tip) in the topmost layer closely mimicks s-SNOM spectroscopic techniques.

Figure 4 shows the intensities of the electromagnetic excitations $S(Q, \omega)$ in the (a) trilayer GR/*h*-BN/GR/Al₂O₃ (b) five-layer GR/*h*-BN/GR/*h*-BN/GR/Al₂O₃ and (c) 21-layer GR/*h*-BN/.../GR/Al₂O₃ obtained with the 2D model. Here the largest carrier doping ($n = 1 \times 10^{14} \text{ e cm}^{-2}$) was chosen so that the modes are more strongly separated and thus easier to analyse. As discussed above, the DP follows a $\omega \propto \sqrt{Q}$ dependence and then saturates due to interband transitions, while the AP mode initially shows the linear-like dependence $\omega \propto Q$ and then bends as it comes closer to the DP. The attenuation of the DP as it bends towards higher energies can be attributed to Landau damping in the interband channel from the continuum of single-particle $\pi \rightarrow \pi^*$ transitions. The effect is more pronounced as more layers are added to the heterostructure as the intensity of the interband transitions increases, but also because the DP dispersion is increasingly steeper and converges to a higher energy. Although it is beyond the scope of this work, we expect that in the bulk limit (i.e. for an infinite number of layers) the DP dispersion completely flattens out to slightly higher energies as is characteristic of a weakly dispersive surface plasmon. Figure 4b demonstrates that the addition of a GR/*h*-BN subunit gives rise to another AP mode. The upper AP mode has an out-of-phase dipolar character—it produces an electric field that oscillates out-of-phase in outer graphenes—while the inner graphene represents the zero field (nodal point). On the other hand, the lower AP exhibits an out-of-phase quadrupolar character as it produces an electric field that oscillates in-phase in outer graphenes which are out-of-phase with the field in the inner graphene. Finally, the highest mode corresponding to the DP exhibits a purely dipolar character producing a field which oscillates in-phase in all three graphenes. Evidently, electromagnetic modes with diverse properties can be achieved by stacking graphene layers. Figure 4c shows the dispersion relation of electromagnetic modes in a 21-layer heterostructure composed of 11 GR and 10 *h*-BN layers. Each added graphene layer represents a new conductive sheet supporting another 2D plasmon. These plasmons hybridise, cluster together and decay in intensity forming an AP series. Interestingly, the DP mode in this case increases sharply to a higher energy exhibiting an almost log-like dependence on Q , while at the same time dropping in intensity as compared to the APs. On the other hand, the lowest energy APs exhibit an almost linear dependence on Q . Although our 2D model can not fully explore the semi-infinite bulk limit, our result nonetheless suggests that the DP converges to the dispersionless surface plasmon when the number of 2D layers becomes infinite. Moreover, we notice the multiplication of the AP which in the bulk case likely converges to a q_z -dependent AP band structure.

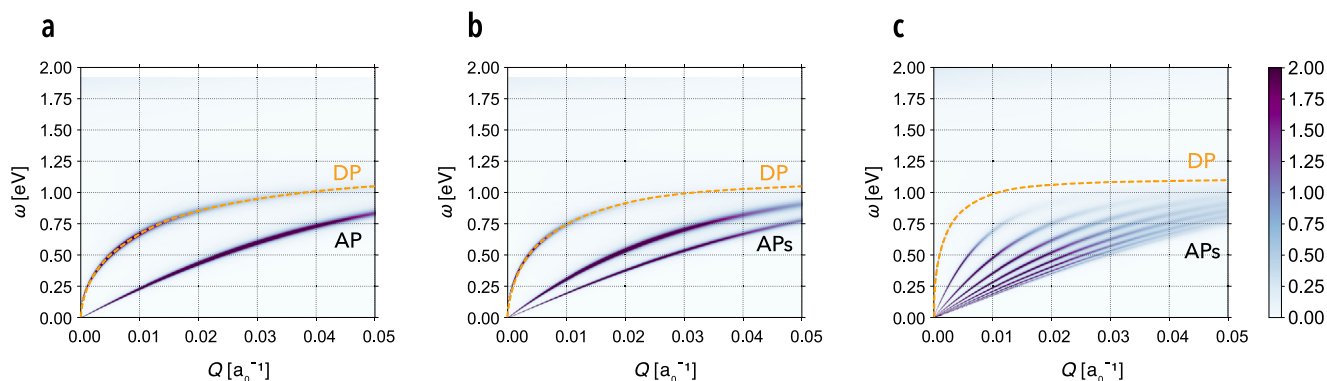


Fig. 4 | Dispersion relations of p(TM) electromagnetic modes in the IR spectrum. Intensities of electromagnetic modes $S_{yy}(\mathbf{Q}, \omega)$ in **a** trilayer GR/h-BN/GR/Al₂O₃, **b** five-layer GR/h-BN/GR/h-BN/GR/Al₂O₃ and **c** 21-layer GR/h-BN/.../GR/Al₂O₃ obtained in the 2D model for the case of strongest doping $n = 1 \times 10^{14} \text{ e cm}^{-2}$. The

number of APs increases by one with each additional graphene layer. The yellow dotted line denotes the dispersion of the Dirac plasmon polariton. All three figures share the same intensity scale.

Bloch plasmon polaritons

Given that the 2D model has proven to be very accurate, especially in the optical limit, we have extended it to explore the case where the top layer is a patterned nanostructure of graphene ribbons. We emphasise that the heterostructure goes beyond the standard GNR/substrate experimental setup^{4,30,45,46}, so that modes appearing in the spectra are a mixture of the inherent GNR plasmon resonances and Bragg-scattered (background) DPs inherent to the bottom graphene sheet. Both effects yield a myriad of plasmonic modes, which will be systematically classified in the subsequent discussion.

Figure 5 shows the intensity of the electromagnetic modes $S_{yy}^{\text{GNR}}(\mathbf{Q}, \omega)$ in the trilayer GNR/h-BN/GR/Al₂O₃. The graphene nanoribbon breaks the xy translational symmetry which introduces its own set of electromagnetic modes called plasmon resonances. Localised plasmon resonances in each GNR are coupled via long-range electromagnetic interaction giving rise to a plasmon resonance band structure. On the other hand, the background DP scatters on the periodic GNR which acts as a grating causing a band-gap opening in the DP dispersion relations, similar to when free electrons are scattered on a periodic crystal potential. Accordingly, we introduce the first Brillouin zone in the transfer wave-vector reciprocal space $Q \in [-\pi/l, \pi/l]$. When the gaped DPs are at the GNR zone boundaries we shall refer to them as Bloch plasmon polaritons (BP1/BP1*). Finally, these Bloch plasmon polaritons and plasmon resonances are mutually coupled. Determining the origin of the newly formed modes in the doped GNR/h-BN/GR/Al₂O₃ trilayer is far from straightforward, due to multiple hybridisation effects influencing the shape of the Bloch DP and plasmon resonance bands and the formation of multiple avoided crossings in the nanoribbon band structure. To isolate/decouple each effect, we performed the calculations by varying the surface charge doping of the top GNR and bottom GR layer independently, as shown in Fig. 5 for:

- a–c increasing doping in the GNR while keeping GR maximally doped,
- d–f increasing GR doping while keeping GNR maximally doped.

In Fig. 5a, the GNR is pristine ($n_{\text{GNR}} \approx 0 \text{ e cm}^{-2}$) and GR is heavily doped ($n_{\text{GR}} = 1 \times 10^{14} \text{ e cm}^{-2}$). In this system, the interaction and thus scattering of the DP on GNR plasmon resonances is very weak. Due to the weak binding, only single Bragg scattering of the DP occurs, so that there is no band-gap opening at the 1st Brillouin zone edges. Therefore, the y -periodicity of nanoribbons only introduces a $2\pi/l$ translation (DP2) and creates mirror images (DP1' and DP2') of the Dirac plasmon (DP1), as illustrated by yellow dotted lines in Fig. 5a. Nonetheless, near 45 meV a faint, seagull-shaped plasmon resonance mode (PR0) appears, as well as another flat plasmon resonance (PR1) at ~55 meV which vanishes near the light cone. A third barely visible resonance can be found at 81 meV, which extends throughout the 1st BZ and vanishes at its edges. These resonances are a consequence of a tiny amount of thermal doping which is present due

to finite temperature effects ($T = 298 \text{ K}$). In addition, we can notice an early hint of DP/PR0 hybridisation as a very narrow but perceptible fall in intensity of PR0 exactly where the yellow dotted line of DP1/DP1' crosses PR0 in the vicinity of the Γ point (as well as at the periodic replicas in the 2nd BZ). However, PR1 and PR2 seem completely unaffected by the presence of the DP.

In Fig. 5b, the nanoribbon is slightly doped ($n_{\text{GNR}} = 1 \times 10^{13} \text{ e cm}^{-2}$) to gradually introduce the hybridisation of DPs and nanoribbon modes. In this case, the strong coupling (and multiple Bragg scattering) occurs which manifests as the splitting of DP1/DP2 (and their mirror DP1'/DP2' modes) into two Bloch plasmon polaritons BP1 and BP1*, with a corresponding band-gap of $\Delta E_{\text{BP1}} = 10 \text{ meV}$ at the 1st BZ boundaries. Near the Γ point one can see the characteristic seagull-shaped PR0 mode now at a higher energy of ~82 meV which has hybridised with the DP forming upper (U-DP/PR0) and lower (L-DP/PR0) polaritonic branches which are periodic with a period of $2\pi/l$.

In Fig. 5c, where the GNR doping is increased to $n_{\text{GNR}} = 2 \times 10^{13} \text{ e cm}^{-2}$ dispersionless resonances (PR0, PR1 and PR2) move to higher energies and even more significantly hybridise with DP1 and DP2. Moreover, one can notice many small gap openings (kinks) up to 300 meV wherever PRs cross the DP dispersion causing them to hybridise and thus bend into many sets of U-DP/PR and L-DP/PR branches. Interestingly, for larger GNR doping, the background DP replica appears very intensively in the GNR absorption spectrum, indicating in a sense the presence of plasmon proximity effects. Moreover, as GNR doping increases, a significant part of the DP intensity is folded into the radiative region, which may be (as we shall see below) tantalising in terms of possible applications. From this we can infer that as doping of the GNR layer increases so does the energy window in which the hybridisation between the Dirac plasmon and ribbon plasmon resonances can occur, opening another avenue for fine-tuning the optical response.

In Fig. 5d, where GNR is strongly doped ($n_{\text{GNR}} = 1 \times 10^{14} \text{ e cm}^{-2}$) and GR is pristine ($n_{\text{GR}} \approx 0 \text{ e cm}^{-2}$) one can observe a very strong seagull-shaped (PR0) and two flat (PR1, PR2) plasmon resonances. The board PR0 mode at ~250 meV and weak and narrow PR2 mode at ~490 meV both exhibit dipolar character, i.e. the y -dependent induced charge density has a single nodal point in the middle of the GNR, making them optically active. On the other hand, the flat PR1 mode at ~300 meV is a plasmon resonance with quadrupolar character whose induced charge density has two nodal points so that PR1 is not an optically active mode (its intensity goes to zero at $Q = 0$). Also, due to weaker quadrupolar inter-GNR interactions, it is less dispersive than the dipolar mode PR0. Given that graphene is slightly thermally doped one can also observe the weak DP squeezed in the 0–60 meV energy region.

By increasing the graphene doping to $n_{\text{GR}} = 1 \times 10^{13} \text{ e cm}^{-2}$, as shown in Fig. 5e, the DP moves to higher energies and hybridise with PR0 causing

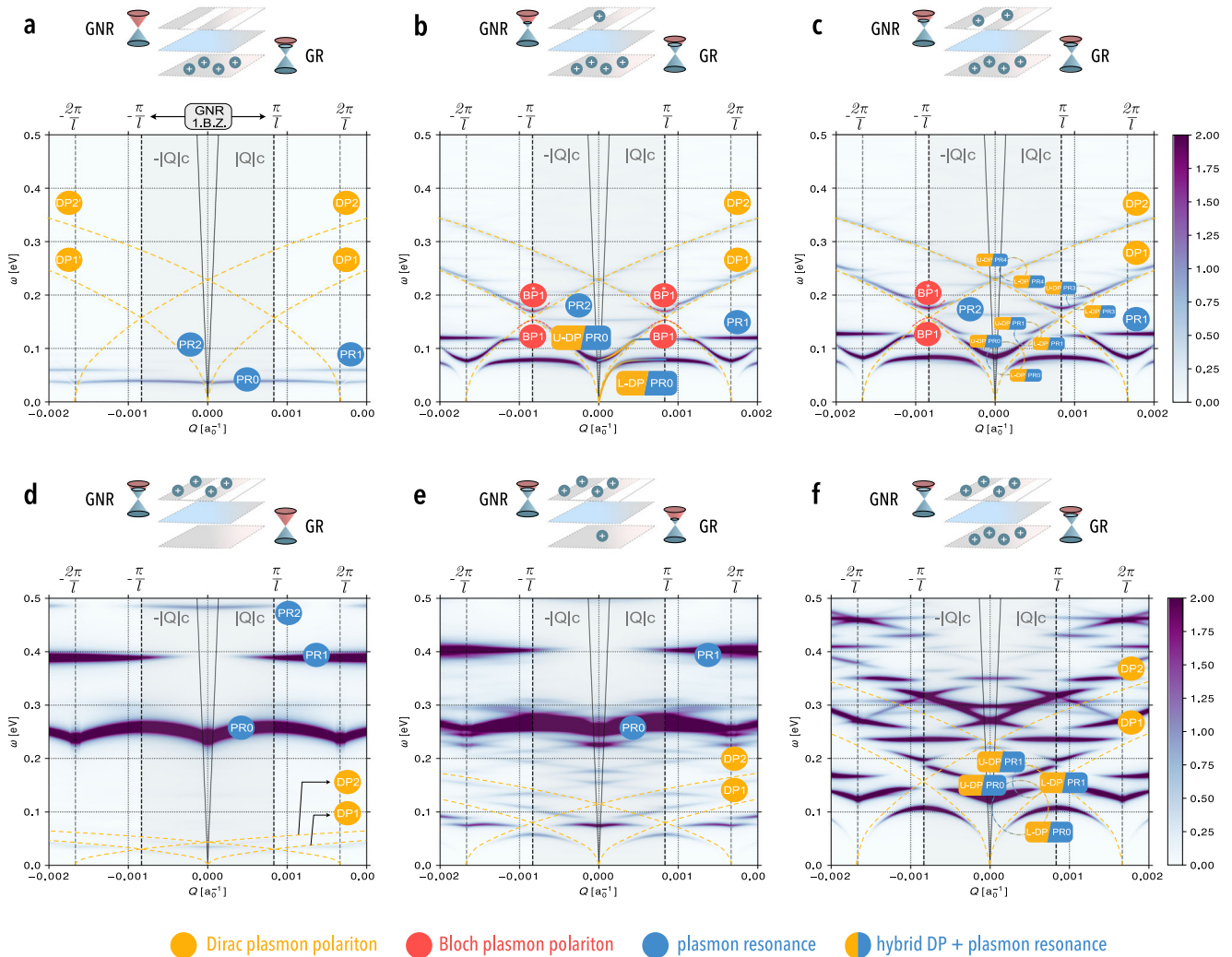


Fig. 5 | Bloch-Dirac plasmon band structure arising in GNR/h-BN/GR/Al₂O₃. Intensities of electromagnetic modes [$S_{yy}^{\text{GNR}}(\mathbf{Q}, \omega)$] as a function of top (n_{GNR}) and bottom (n_{GR}) layer charge carrier doping. **a** $n_{\text{GNR}} = 0 \text{ e cm}^{-2}$, $n_{\text{GR}} = 1 \times 10^{14} \text{ e cm}^{-2}$ **b** $n_{\text{GNR}} = 1 \times 10^{13} \text{ e cm}^{-2}$, $n_{\text{GR}} = 1 \times 10^{14} \text{ e cm}^{-2}$ **c** $n_{\text{GNR}} = 2 \times 10^{13} \text{ e cm}^{-2}$, $n_{\text{GR}} = 1 \times 10^{14} \text{ e cm}^{-2}$ **d** $n_{\text{GNR}} = 1 \times 10^{14} \text{ e cm}^{-2}$, $n_{\text{GR}} = 0 \text{ e cm}^{-2}$ **e** $n_{\text{GNR}} = 1 \times 10^{14} \text{ e cm}^{-2}$, $n_{\text{GR}} = 1 \times 10^{13} \text{ e cm}^{-2}$ **f** $n_{\text{GNR}} = 1 \times 10^{14} \text{ e cm}^{-2}$, $n_{\text{GR}} = 1 \times 10^{14} \text{ e cm}^{-2}$. The Dirac plasmons DP1/DP2' and DP1'/DP2 in the bottom GR layer (yellow) scatter on topmost GNR forming Bloch plasmon polariton modes BP1 and BP1* (red). The GNR by itself supports plasmon resonances PR0, PR1, PR2,... (blue) which hybridise with DP1/DP2' and DP1'/DP2 to form lower (L-DP) and upper (U-DP) polaritonic branches (yellow+blue). Hybridisation is controlled by doping of the bottom GR and the top GNR layer. When doping is set to zero, thermal doping is still present due to finite temperature effects $T = 298 \text{ K}$. Black dashed lines represent the ribbon Brillouin zone boundaries $Q = \pm \pi/L$, while the grey lines represent the light cone ($\pm|Qc|$). Dirac cones above each plot illustrate the doping level of each layer. All six figures share the same intensity scale and are symmetric w.r.t. $Q = 0 \text{ a}_0^{-1}$.

the distortion of its seagull shape. Also, the energies of PR0 and PR1 are slightly increased and smear out over a slightly broader range. In this case, PR2 energy has increased by about ~60 meV, pushing it beyond the observed energy range. In addition, the Bloch plasmon band structure begins to emerge below 200 meV and a clear band-gap opening can be seen between BP1 and BP1*.

Finally, Fig. 5f shows the intensity of the electromagnetic modes when both top and bottom layers are strongly doped ($n_{\text{GNR}} = n_{\text{GR}} = 1 \times 10^{14} \text{ e cm}^{-2}$) resulting in a combination of all effects from Fig. 5a to e. The yellow dashed line representing the uncoupled DP1 and DP2 in these figures is only shown for easier visual interpretation as those modes are now fully hybridised. Evidently, strong doping enables a whole variety of plasmonic modes, some of which are evanescent $\omega > Qc$, while others fall into the radiative region $\omega \geq Qc$ and become IR active. In fact, there is a whole cacophony of plasmonic bands appearing at: $\omega \sim 120 \text{ meV}$, 215 meV, 265 meV, 300 meV, 350 meV, etc., which can be directly excited by infrared radiation. For example, the intensive radiative

mode at $\omega \sim 120 \text{ meV}$ is a standard optically active GNR PR, while the large seagull-shaped patterns at $\omega \sim 260 \text{ meV}$ and $\sim 300 \text{ meV}$ represent the Bragg-folded DP. This latter case is especially intriguing. Namely, the seagull-shaped pattern covers a very large fraction of the background DP which is folded into the radiative region and thus replicated in the GNR optical absorption spectrum. In other words, this system enables direct excitation of very strong DP by IR radiation, making it extraordinarily useful in optoelectronic applications. We also observe that strong coupling of DP to the GNR grating results in the bending of the DP into arcs (in the energy region $\omega \leq 100 \text{ meV}$) representing the Bloch plasmon BP1 which repeats periodically with a period of $2\pi/l$. Moreover, due to hybridisation with GNR plasmon resonances, the upper Bloch plasmon branch BP1* is barely visible at the BZ edge ($Q = \pm \pi/l$). Nevertheless, we estimate a band-gap opening of $\Delta E_{\text{BP1}} \approx 85 \text{ meV}$. In the gap between BP1 and BP1* one can notice the nanoribbon plasmon resonances, which extend through extended BZs, but precisely in such a way that they resemble the DP1 and DP2 square-root dependence ($\propto \sqrt{Q}$), albeit shifted to higher energies. It should be

emphasised that DP1 and DP2 plasmons are inherent to the background (bottom) GR and not the (top) nanoribbon graphene layer. In other words, the same pattern would appear in the spectrum in the absence of the nanoribbon⁴⁷.

Finally, all these plasmon resonances can be tuned on-demand, as it is straightforward to modify both the ribbon width^{4,30,45,48}, as well as the doping of each layer. As expected this property means GNR/*h*-BN/GR contains an integrated nano-scale diffraction grating which could pave way for many attractive applications in terahertz electronics, optoelectronics (emitters, photovoltaics, sensors) and sub-diffraction optics^{5,25,49-54}.

Discussion

A versatile and computationally efficient theoretical model (based on a fully ab initio RPA optical conductivity tensor) for predicting on-demand optical properties of multilayer vdW heterostructures was developed and applied on GR/*h*-BN/GR/... composite systems. The multifaceted tuning of the dispersion relation of surface plasmon polariton modes by varying the number of layers in GR/*h*-BN van der Waals heterostructures, as well as electrostatic doping and patterning of graphene layer into graphene nanoribbons was demonstrated. The inclusion of the dielectric substrate was shown to be straightforward, as was demonstrated for Al₂O₃, and thus provided a far more realistic depiction of the system. The computationally extremely efficient 2D model enabled the exploration of limiting behaviour in the SPP dispersion from trilayer graphene/*h*-BN to surface bulk composed of 21 layers. The systematic classification of plasmon polariton modes in GR/*h*-BN/GR/Al₂O₃ and in GNR/*h*-BN/GR/Al₂O₃ heterostructure was provided; allowing for a clear distinction between Dirac and acoustic plasmon polaritons, as well as plasmon resonances and Bloch plasmon polaritons, respectively. In addition, we quantified the BP band-gap opening. Furthermore, our calculations predicted very efficient Umklapp scattering of the DP into the radiative region leading to its conversion into a strong IR active mode. We have shown that the intensity and frequency of the BP mode can be tuned by biasing the bottom graphene layer, as well as the topmost GNR, which significantly facilitates the frequency-tuning process and achievement of different plasmonic properties. This phenomenon is yet to be examined experimentally, but its investigation should pose no significant challenge, as the synthesis of multilayer and graphene ribbons has already become routine. In future work, the developed model (including ladder corrections to the RPA photon self-energy) could be easily applied to explore electromagnetic modes in the semiconducting composites (such as TMD/*h*-BN heterostructures) to investigate the strong exciton-photon coupling. In addition, the formalism could be extended to include the coupling between DP in graphene and widely studied hyperbolic phonon polaritons in hexagonal boron nitride^{2,17,55}.

Methods

Theoretical formulation

The quantity from which we shall extract the pieces of information about the electromagnetic modes in GR/*h*-BN nanostructures is the electrical field propagator $\mathcal{E}_{\mu\nu}$. The electrical field produced by an external oscillating point dipole $\mathbf{p}_0 e^{-i\omega t}$ placed in point \mathbf{r}' is defined as⁵⁶

$$E_{\mu}(\mathbf{r}, \omega) = \sum_{\nu=x,y,z} \mathcal{E}_{\mu\nu}(\mathbf{r}, \mathbf{r}', \omega) p_{\nu}^0, \quad (3)$$

where $\mathcal{E}_{\mu\nu}$ can be connected with the time-ordered photon propagator $D_{\mu\nu} = \frac{i}{\hbar c} \langle T \{ A_{\mu} A_{\nu} \} \rangle$ as $\mathcal{E}_{\mu\nu} = \frac{i\omega}{c} D_{\mu\nu}$. Due to the aforesaid, the electric field

propagator satisfies Dyson's equation $\mathcal{E} = \Gamma + \Gamma \sigma \mathcal{E}$, where σ represents the conductivity tensor (or photon self-energy) of GR/*h*-BN nanostructure, and Γ represents the propagator of electrical field in the absence of GR/*h*-BN nanostructure, i.e. when $\sigma = 0$ ^{14,38}. Considering that the wavelength of the electromagnetic modes considered here ($\lambda = 2\pi/Q > 100 \text{ \AA}$) will be much larger than the crystal unit cell in parallel *xy* direction ($a \sim 2.5 \text{ \AA}$) we shall neglect the dispersivity of the dynamic response within crystal unit cell in *xy* plane. However, we shall retain the important effects coming from the dispersion of the dynamic response in the direction perpendicular to GR/*h*-BN nanostructures (*z* direction). Therefore, the conductivity tensor σ will be considered as translationally invariant in the *xy* plane while its dispersivity in the *z* direction will be considered exactly or within 2D approximation. This also means that the crystal local field effects will be neglected in the *xy* plane but will be (at different levels of approximation) included in the *z* direction. After imposing the planar symmetry of the GR/*h*-BN heterostructure, the Dyson equation for the propagator \mathcal{E} becomes explicitly

$$\begin{aligned} \mathcal{E}_{\mu\nu}(\mathbf{Q}, \omega, z, z') &= \Gamma_{\mu\nu}(\mathbf{Q}, \omega, z, z') + \\ &\sum_{\alpha,\beta=x,y,z} \int_{-L/2}^{L/2} dz_1 \int_{-L/2}^{L/2} dz_2 \Gamma_{\mu\alpha}(\mathbf{Q}, \omega, z, z_1) \\ &\sigma_{\alpha\beta}(\mathbf{Q}, \omega, z_1, z_2) \mathcal{E}_{\beta\nu}(\mathbf{Q}, \omega, z_2, z'), \end{aligned} \quad (4)$$

where $\mathbf{Q} = (Q_x, Q_y)$ and ω are the transfer wavevector and frequency, respectively. The propagator of the electrical field, in the absence of GR/*h*-BN nanostructure, can be written as

$$\Gamma = \Gamma^0 + \Gamma^{\text{sc}}, \quad (5)$$

where the propagator of the 'free' electric field (or free photon propagator) is^{14,56,57}

$$\Gamma^0(\mathbf{Q}, \omega, z, z') = -\frac{4\pi i}{\epsilon_0 \omega} \delta(z - z') \mathbf{z} \cdot \mathbf{z} - \frac{2\pi\omega}{\beta_0 c^2} e^{i\beta_0 |z - z'|} \sum_{q=s,p} \mathbf{e}_q^0 \cdot \mathbf{e}_q^0. \quad (6)$$

The propagator of the electric field scattered by the dielectric substrate, in the region $z > z_s$, is given by⁵⁶

$$\Gamma^{\text{sc}}(\mathbf{Q}, \omega, z, z') = -\frac{2\pi\omega}{\beta_0 c^2} e^{i\beta_0(z+z')} \sum_{q=s,p} r_q \cdot \mathbf{e}_q^+ \cdot \mathbf{e}_q^-. \quad (7)$$

Here the unit vectors of the s(TE) polarised electromagnetic field are $\mathbf{e}_s^{0,\pm} = \mathbf{Q}_0 \times \mathbf{z}$. The unit vectors of p(TM) polarised electromagnetic field are $\mathbf{e}_p^{0,\pm} = \frac{c}{\omega\sqrt{\epsilon_0}} [\alpha_{0,\pm} \beta_0 \mathbf{Q}_0 + Q\mathbf{z}]$, where $\alpha_0 = -\text{sgn}(z - z')$, $\alpha_{\pm} = \mp 1$, and \mathbf{Q}_0 and \mathbf{z} are the unit vectors in the \mathbf{Q} and *z* directions, respectively. The reflection coefficients of the s(TE) and p(TM) polarised electromagnetic waves at the media/substrate interface are $r_s = (\beta_0 - \beta_s)/(\beta_0 + \beta_s)$ and $r_p = (\beta_0 \epsilon_s - \beta_s \epsilon_0)/(\beta_0 \epsilon_s + \beta_s \epsilon_0)$, respectively. The complex wave vectors in the perpendicular (*z*) direction are

$$\beta_{0,s} = \sqrt{\frac{\omega^2}{c^2} \epsilon_{0,s}(\omega) - Q^2}. \quad (8)$$

For simplicity, from now on, we assume that the dielectric media is a vacuum, i.e. $\epsilon_0 = 1$.

Calculation of propagator $\mathcal{E}_{\mu\nu}(\omega)$ in the atomistic model. The approximation of translational invariance in the *xy* plane results that the Fourier transform of the conductivity tensor can be approximated as

$$\sigma_{\mu\nu, G, G'}(\mathbf{Q}, \omega) \approx \sigma_{\mu\nu, G_z, G'_z}(\mathbf{Q}, \omega) \delta_{G_0} \delta_{G'_0} \quad (9)$$

so that its Fourier expansion in z direction becomes

$$\sigma_{\mu\nu}(\mathbf{Q}, \omega, z, z') = \frac{1}{L} \sum_{G_z} \sum_{G'_z} e^{iG_z z} e^{-iG'_z z'} \sigma_{\mu\nu, G_z G'_z}(\mathbf{Q}, \omega), \quad (10)$$

where $\mathbf{G} = (\mathbf{G}_{\parallel}, G_z)$ are 3D reciprocal vectors and L is unit cell in the z direction. The Fourier transform of RPA conductivity tensor of entire GR/ h -BN/GR heterostructure is¹⁴

$$\sigma_{\mu\nu, \mathbf{G}\mathbf{G}'}(\mathbf{Q}, \omega) = -\frac{2i\hbar}{\Omega} \sum_{\mathbf{K}, n, m} \frac{1}{E_{n\mathbf{K}} - E_{m\mathbf{K}+\mathbf{Q}}} \frac{f_{n\mathbf{K}} - f_{m\mathbf{K}+\mathbf{Q}}}{\hbar\omega + i\eta + E_{n\mathbf{K}} - E_{m\mathbf{K}+\mathbf{Q}}} \times \int_{n\mathbf{K}, m\mathbf{K}+\mathbf{Q}}^{\mu}(\mathbf{G}) [j_{n\mathbf{K}, m\mathbf{K}+\mathbf{Q}}^{\nu}(\mathbf{G}')]^*, \quad (11)$$

were the current vertices are

$$j_{n\mathbf{K}, m\mathbf{K}+\mathbf{Q}}^{\mu}(\mathbf{G}) = \int_{\Omega} d\mathbf{r} e^{-i(\mathbf{Q}+\mathbf{G})\mathbf{r}} j_{n\mathbf{K}, m\mathbf{K}+\mathbf{Q}}^{\mu}(\mathbf{r}), \quad (12)$$

and the current produced by transitions between Bloch states $\phi_{n\mathbf{K}}^* \rightarrow \phi_{m\mathbf{K}+\mathbf{Q}}$ are defined as

$$j_{n\mathbf{K}, m\mathbf{K}+\mathbf{Q}}^{\mu}(\mathbf{r}) = \frac{e\hbar}{2im} \left\{ \phi_{n\mathbf{K}}^*(\mathbf{r}) \partial_{\mu} \phi_{m\mathbf{K}+\mathbf{Q}}(\mathbf{r}) - [\partial_{\mu} \phi_{n\mathbf{K}}^*(\mathbf{r})] \phi_{m\mathbf{K}+\mathbf{Q}}(\mathbf{r}) \right\}. \quad (13)$$

Here $\Omega = S \times L$ and S are the normalisation volume and surface, respectively, while $\mathbf{K} = (K_x, K_y)$ is the 2D wave vector, $\phi_{n\mathbf{K}}$ and $E_{n\mathbf{K}}$ are Bloch wave functions and energies obtained in the ground state DFT calculation, and $f_{n\mathbf{K}} = [e^{(E_{n\mathbf{K}} - E_F)/kT} + 1]^{-1}$ is the Fermi-Dirac distribution at temperature T . Here η represents the phenomenological damping parameter. After the Fourier expansion (Eq. (10)) and the same Fourier expansion for Γ^0 and \mathcal{E} are inserted in (Eq. (4)), it becomes a matrix equation

$$\begin{aligned} \mathcal{E}_{\mu\nu, G_z G'_z}(\mathbf{Q}, \omega) &= \Gamma_{\mu\nu, G_z G'_z}^0(\mathbf{Q}, \omega) \\ &+ \sum_{\alpha, \beta=x, y, z} \sum_{G_{z1}, G_{z2}} \Gamma_{\mu\alpha, G_z G_{z1}}^0(\mathbf{Q}, \omega) \sigma_{\alpha\beta, G_{z1}, G_{z2}}(\mathbf{Q}, \omega) \mathcal{E}_{\beta\nu, G_{z2}, G'_z}(\mathbf{Q}, \omega), \end{aligned} \quad (14)$$

where the free photon propagator matrix is defined as

$$\Gamma_{\alpha\beta, G_{z1}, G_{z2}}^0(\mathbf{Q}, \omega) = \frac{1}{L} \int_{-L/2}^{L/2} e^{-iG_{z1} z} \Gamma_{\alpha\beta}^0(\mathbf{Q}, \omega, z, z') e^{iG_{z2} z'} dz dz'. \quad (15)$$

Once we solve the matrix equation, Eq. (14), we obtain the \mathcal{E} tensor. The spectra of surface electromagnetic modes are then defined as

$$S_{\mu\nu}(\mathbf{Q}, \omega) = -\text{Re}\{\mathcal{E}\}_{\mu\nu}(\mathbf{Q}, \omega), \quad (16)$$

where the surface electrical field propagator is defined as

$$\begin{aligned} \mathcal{E}_{\mu\nu}(\mathbf{Q}, \omega) &= \mathcal{E}_{\mu\nu}(\mathbf{Q}, \omega, z = z_1, z' = z_1) \\ &= \frac{1}{L} \sum_{G_z} \sum_{G'_z} e^{iG_z z_1} e^{-iG'_z z_1} \mathcal{E}_{\mu\nu, G_z G'_z}(\mathbf{Q}, \omega), \end{aligned} \quad (17)$$

i.e. as the dipolar electric field in the topmost graphene layer at $z = z_1$.

Calculation of propagator $\mathcal{E}_{\mu\nu}(\omega)$ in the 2D model. The first assumption required to implement the 2D model is that the ground state electronic structure of each self-standing 2D crystal (i.e. layer), forming the heterostructure, is weakly affected when they are stacked in a vdW heterostructure. Figure 2 undoubtedly confirms that this is for example the case in GR/ h -BN/GR heterostructures. This makes it possible to calculate the electromagnetic response of the entire heterostructures in two steps:

1. the calculation of conductivity tensor for each type of self-standing 2D crystals σ' which is part of the heterostructure;
2. stacking the σ' s in the heterostructure and calculating their mutual screening via the photon propagator Γ .

Moreover, since here we are interested in the electromagnetic modes in the visible (VIS) and IR frequency regions, i.e., $\hbar\omega < 2$ eV, according to Eq. (8), the maximum wavelength in the perpendicular direction $\lambda = 2\pi c/\omega$ is incomparably larger than the thickness of self-standing 2D crystals (graphene or h -BN) so that their conductivities can be approximated by local 2D conductivities

$$\sigma_{\mu\nu}^i(\mathbf{Q}, \omega, z, z') \approx \sigma_{\mu\mu}^i(\omega) \delta_{\mu\nu} \delta(z - z_i) \delta(z' - z_i). \quad (18)$$

The local conductivity of the i th 2D layer is defined as¹⁴

$$\sigma_{\mu\mu}^i(\omega) = L_i \sigma_{\mu\mu, \mathbf{G}=0 \mathbf{G}'=0}^i(\mathbf{Q} = 0, \omega), \quad (19)$$

where $\sigma_{\mu\nu, \mathbf{G}\mathbf{G}'}^i(\mathbf{Q}, \omega)$ represents the full microscopic conductivity of 2D crystal, given by (Eq. (11)), and L_i is vertical (z) lattice parameter in the DFT ground state calculation of i th 2D crystal. Furthermore, the RPA 2D conductivity of i th crystal can be split into intraband and interband contributions explicitly

$$\sigma_{\mu\mu}^i(\mathbf{Q}, \omega) = \sigma_{\mu\mu}^{\text{intra}, i}(\omega) + \sigma_{\mu\mu}^{\text{inter}, i}(\mathbf{Q}, \omega). \quad (20)$$

Here the intraband ($n = m$) contribution is simply the Drude conductivity

$$\sigma_{\mu\mu}^{\text{intra}}(\omega) = i \frac{e^2}{m} \frac{n_{\mu\mu}}{\omega + i\eta_{\text{intra}}}, \quad (21)$$

where the effective number of charge carrier is

$$n_{\mu\mu} = -\frac{m}{Se^2} \sum_n \sum_{\mathbf{K} \in 1.\text{SBZ}} \frac{\partial f_{n\mathbf{K}}}{\partial E_{n\mathbf{K}}} |j_{n\mathbf{K}, n\mathbf{K}}^{\mu}(\mathbf{G} = 0)|^2. \quad (22)$$

While the interband ($n \neq m$) conductivity is defined as

$$\sigma_{\mu\mu}^{\text{inter}}(\mathbf{Q}, \omega) = -i \frac{\hbar}{S} \sum_{n \neq m} \sum_{\mathbf{K} \in 1.\text{SBZ}} \frac{f_{n\mathbf{K}} - f_{m\mathbf{K}+\mathbf{Q}}}{E_{n\mathbf{K}} - E_{m\mathbf{K}+\mathbf{Q}}} \frac{|j_{n\mathbf{K}, m\mathbf{K}+\mathbf{Q}}^{\mu}(\mathbf{G} = 0)|^2}{\hbar\omega + E_{n\mathbf{K}} - E_{m\mathbf{K}+\mathbf{Q}} + i\eta_{\text{inter}}}. \quad (23)$$

Correspondingly, the conductivity of the entire heterostructure in the 2D approximation is

$$\sigma_{\mu\nu}(\mathbf{Q}, \omega, z, z') = \sum_{i=1}^n \sigma_{\mu\nu}^i(\mathbf{Q}, \omega, z, z') = \sum_i \sigma_{\mu\mu}^i(\omega) \delta_{\mu\nu} \delta(z - z_i) \delta(z' - z_i). \quad (24)$$

We note in passing that this summation procedure leads to the neglect of interlayer hybridisation which has a negligible effect due to the exponential decay of the induced field outside of each layer. After setting $z = z_i$ and $z' = z_j$ and inserting the conductivity (Eq. (24)) in Eq. (4), we obtain the matrix equation for the propagator of the electrical field between the points placed within 2D layers (z_i, z_j)

$$\begin{aligned} \mathcal{E}_{\mu\nu}(\mathbf{Q}, \omega, z_i, z_j) &= \Gamma_{\mu\nu}(\mathbf{Q}, \omega, z_i^{\dagger}, z_j) \\ &+ \sum_{\alpha, \beta=x, y, z} \sum_{kl=1}^n \Gamma_{\mu\alpha}(\mathbf{Q}, \omega, z_i^{\dagger}, z_k) \sigma_{\alpha\beta}^{kl}(\omega) \mathcal{E}_{\beta\nu}(\mathbf{Q}, \omega, z_l, z_j), \end{aligned} \quad (25)$$

where $\sigma_{\alpha\beta}^{kl}(\omega) = \sigma_{\alpha\alpha}^k(\omega) \delta_{\alpha\beta} \delta_{kl}$. Here we assume that substrate is included in calculations, so according to (Eqs. (5) to (7)) and if we choose $\mathbf{Q} = \mathbf{y}$ the

propagator Γ is explicitly

$$\Gamma(\mathbf{Q}, \omega, z_i^+, z_j) = \begin{bmatrix} \Gamma_{xx}^0 & 0 & 0 \\ 0 & \Gamma_{yy}^0 & \Gamma_{yz}^0 \\ 0 & \Gamma_{yz}^0 & \Gamma_{zz}^0 \end{bmatrix} e^{i\beta_0|z_i - z_j|} + \begin{bmatrix} \Gamma_{xx}^{\text{sc}} & 0 & 0 \\ 0 & \Gamma_{yy}^{\text{sc}} & \Gamma_{yz}^{\text{sc}} \\ 0 & -\Gamma_{yz}^{\text{sc}} & \Gamma_{zz}^{\text{sc}} \end{bmatrix} e^{i\beta_0(z_i + z_j)}, \quad (26)$$

where $\Gamma_{xx}^0 = -\frac{2\pi\omega}{c^2\beta_0}$, $\Gamma_{yy}^0 = -\frac{2\pi\beta_0}{\omega}$, $\Gamma_{zz}^0 = -\frac{2\pi Q^2}{\omega} \Gamma^0 = \frac{2\pi Q}{\omega} \text{sgn}(z_i - z_j)$, $\Gamma_{xx}^{\text{sc}} = \Gamma_{xx}^0 r_s$, $\Gamma_{yy}^{\text{sc}} = -\Gamma_{yy}^0 r_p$, $\Gamma_{zz}^{\text{sc}} = \Gamma_{zz}^0 r_p$ and $\Gamma_{yz}^{\text{sc}} = \frac{\beta_0 Q}{\omega} r_p$. Here $z_i^+ = z_i + \delta$ (where δ is an infinitesimally small positive number) eliminates the local term in $\Gamma_{zz}^0(z, z')$. After solving the matrix equation Eq. (25), we obtain the $\mathcal{E}_{\mu\nu}^{\text{GNR}}(z_i, z_j)$ components. The spectra of surface electromagnetic modes are also defined as Eq. (16), where by analogy with Eq. (17) the surface electrical field propagator is defined as

$$\mathcal{E}_{\mu\nu}(\mathbf{Q}, \omega) = \mathcal{E}_{\mu\nu}(\mathbf{Q}, \omega, z_n, z_n), \quad (27)$$

i.e. as the dipole electric field in the topmost (n -th) 2D layer.

It should be emphasised that the 2D conductivity defined by Eq. (19) contains only the monopolar contribution to the induced current density (i.e., only the dipolar contribution to the induced charge density), which would correspond to keeping only the dipolar contribution in the density response functions (Eq. (2) of ref. 37). The plausibility of this approximation, in addition to the already well-established agreement with the atomistic model, can be confirmed by using a computationally more intensive *quasi-2D approximation*⁵⁸. In this approximation, the full spatial dispersivity and non-local character of partial conductivities $\sigma_{\mu\nu}^i(z, z')$ is retained, or more formally, instead of using the approximation in Eq. (18), we use $\sigma_{\mu\nu}^i(\mathbf{Q}, \omega, z, z') = \sigma_{\mu\nu}^i(\mathbf{Q}, \omega, z - z_i, z' - z_i)$. Then according to Eq. (24) the total conductivity becomes $\sigma_{\mu\nu}(\mathbf{Q}, \omega, z, z') = \sum_i \sigma_{\mu\nu}^i(\mathbf{Q}, \omega, z - z_i, z' - z_i)$. After this conductivity is Fourier transformed (w.r.t. the multilayer unit supercell L) and inserted in Eq. (14), the obtained intensities of the electromagnetic modes are almost identical to the ones determined by using Eq. (18) for all wavenumbers up to $Q \leq 0.05$ a. u. This implies that contributions to the induced current from all higher multipoles beyond the dipole have no effect on the electromagnetic modes in this Q range.

Calculation of propagator $\mathcal{E}_{\mu\nu}^{\text{GNR}}(\omega)$ in the GNR/h-BN/GR nanostructure 2D model. Suppose that the topmost graphene layer at $z = z_1$ is patterned into graphene nanoribbons of width d and a period l (see last panel of Fig. 1a). This causes electromagnetic field fluctuations inherent to the background heterostructure $B \equiv h\text{-BN/GR/Al}_2\text{O}_3$ to be scattered by current fluctuations in the GNR. In other words, in the presence of the GNR, the propagator of electromagnetic modes satisfies the following Dyson equation

$$\mathcal{E}^{\text{GNR}}(\mathbf{r}, \mathbf{r}', \omega) = \mathcal{E}^0(\mathbf{r}, \mathbf{r}', \omega) + \int d\mathbf{r}_1 d\mathbf{r}_2 \mathcal{E}^0(\mathbf{r}, \mathbf{r}_1, \omega) \sigma^{\text{GNR}}(\mathbf{r}_1, \mathbf{r}_2, \omega) \mathcal{E}^{\text{GNR}}(\mathbf{r}_2, \mathbf{r}', \omega), \quad (28)$$

where σ^{GNR} is the GNR nonlocal conductivity and \mathcal{E}^0 now represents the electrical field propagator in the $h\text{-BN/GR/Al}_2\text{O}_3$ heterostructure. In other words, the propagator \mathcal{E}^0 satisfies an equation analogous to Eq. (28), i.e. $\mathcal{E}^0 = \Gamma + \Gamma \sigma^{\text{B}} \mathcal{E}^0$, where σ^{B} represents the nonlocal conductivity of the background heterostructure $B \equiv h\text{-BN/GR/Al}_2\text{O}_3$. According to the previously mentioned local and 2D approximation, the conductivity tensor, describing current fluctuations in the GNR, can be written as

$$\sigma_{\mu\nu}^{\text{GNR}}(\mathbf{r}, \mathbf{r}', \omega) \approx \delta(z - z_1) \sigma_{\mu\nu}^{\text{GNR}}(y, \omega) \delta(\mathbf{r} - \mathbf{r}'), \quad (29)$$

where the periodic part of conductivity can be approximated as

$$\sigma_{\mu\nu}^{\text{GNR}}(y, \omega) = \sigma_{\mu\nu}(\omega) \sum_{n=-\infty}^{n=\infty} [\theta(y - nl + d/2) - \theta(y - nl - d/2)], \quad (30)$$

and where $\sigma_{\mu\nu}(\omega)$ is local conductivity of single-layer graphene derived from Eq. (19). Due to Bragg scattering on a periodic GNR grating, the propagator \mathcal{E}^{GNR} is no longer translationally invariant in the xy direction so that its Fourier expansion becomes

$$\mathcal{E}_{\mu\nu}^{\text{GNR}}(\mathbf{r}, \mathbf{r}', \omega) = \sum_{\mathbf{g}} \int \frac{d\mathbf{Q}}{(2\pi)^2} \mathcal{E}_{\mu\nu, \mathbf{g}\mathbf{g}'}^{\text{GNR}}(\mathbf{Q}, \omega, z, z') e^{i(\mathbf{Q}+\mathbf{g})\rho} e^{-i(\mathbf{Q}+\mathbf{g}')\rho'}, \quad (31)$$

where the 2D reciprocal vectors are $\mathbf{g} = (0, g)$, with $g = \frac{2\pi k}{l}$; $k = 0 \pm 1, \pm 2, \dots$ and $\rho = (x, y)$ is the 2D position vector. The background electrical field propagator \mathcal{E}^0 remains translationally invariant in the xy plane, however, we want to retain the same form of its Fourier expansion

$$\mathcal{E}_{\mu\nu}^0(\mathbf{r}, \mathbf{r}', \omega) = \sum_{\mathbf{g}} \int \frac{d\mathbf{Q}}{(2\pi)^2} \mathcal{E}_{\mu\nu, \mathbf{g}\mathbf{g}'}^0(\mathbf{Q}, \omega, z, z') e^{i(\mathbf{Q}+\mathbf{g})\rho} e^{-i(\mathbf{Q}+\mathbf{g}')\rho'}, \quad (32)$$

where

$$\mathcal{E}_{\mu\nu, \mathbf{g}\mathbf{g}'}^0(\mathbf{Q}, \omega, z, z') = \mathcal{E}_{\mu\nu}^0(\mathbf{Q} + \mathbf{g}, \omega, z, z') \delta_{\mathbf{g}\mathbf{g}'}. \quad (33)$$

After the expressions (Eqs. (29) to (33)) are inserted into Dyson's equation (Eq. (28)) it transforms into the following (spatial) matrix equation for the scattered propagator

$$\mathcal{E}_{\mu\nu, \mathbf{g}\mathbf{g}'}^{\text{GNR}}(\mathbf{Q}, \omega, z, z') = \mathcal{E}_{\mu\nu, \mathbf{g}\mathbf{g}'}^0(\mathbf{Q}, \omega, z, z') + \sum_{\alpha\beta} \sum_{\mathbf{g}_1 \mathbf{g}_2} \mathcal{E}_{\mu\alpha, \mathbf{g}\mathbf{g}_1}^0(\mathbf{Q}, \omega, z, z_1) \sigma_{\alpha\beta, \mathbf{g}_1 \mathbf{g}_2}^{\text{GNR}}(\omega) \mathcal{E}_{\beta\nu, \mathbf{g}_2 \mathbf{g}'}^{\text{GNR}}(\mathbf{Q}, \omega, z_1, z'), \quad (34)$$

where the conductivity matrix is

$$\sigma_{\mu\nu, \mathbf{g}\mathbf{g}'}^{\text{GNR}}(\omega) = \sigma_{\mu\nu}(\omega) \times \begin{cases} \frac{2}{l(g-g')} \sin[(g-g')d/2]; & g \neq g' \\ d/l; & g = g' \end{cases}. \quad (35)$$

After inserting $z = z' = z_1$ we obtain the pure matrix equation for the propagator of the scattered electrical field inside the GNR plane

$$\mathcal{E}_{\mu\nu, \mathbf{g}\mathbf{g}'}^{\text{GNR}}(\mathbf{Q}, \omega, z_1, z_1) = \mathcal{E}_{\mu\nu, \mathbf{g}\mathbf{g}'}^0(\mathbf{Q}, \omega, z_1, z_1) + \sum_{\alpha\beta} \sum_{\mathbf{g}_1 \mathbf{g}_2} \mathcal{E}_{\mu\alpha, \mathbf{g}\mathbf{g}_1}^0(\mathbf{Q}, \omega, z_1, z_1) \sigma_{\alpha\beta, \mathbf{g}_1 \mathbf{g}_2}^{\text{GNR}}(\omega) \mathcal{E}_{\beta\nu, \mathbf{g}_2 \mathbf{g}'}^{\text{GNR}}(\mathbf{Q}, \omega, z_1, z_1). \quad (36)$$

The ingredients required to solve this equation are; matrix σ^{GNR} , defined explicitly by Eq. (35) and the matrix \mathcal{E}^0 which is according to (Eq. (33)) defined as

$$\mathcal{E}_{\mu\nu, \mathbf{g}\mathbf{g}'}^0(\mathbf{Q}, \omega, z_1, z_1) = \mathcal{E}_{\mu\nu}^0(\mathbf{Q} + \mathbf{g}, \omega, z_1, z_1) \delta_{\mathbf{g}\mathbf{g}'}. \quad (37)$$

In the atomistic model the propagator of the background electrical field $\mathcal{E}_{\mu\nu}^0(\mathbf{Q}, \omega, z_1, z_1)$ is exactly equal to the surface electrical field propagator (Eq. (17)), which is obtained by solving Dyson's equation (Eq. (14)) in which enters the conductivity tensor (Eq. (11)) calculated for the $h\text{-BN/GR}$ bilayer, i.e. for the $GR/h\text{-BN/GR}$ composite in which the topmost atomic layer is simply removed. Here we adopt the 2D model, where the background field propagator $\mathcal{E}_{\mu\nu}^0(\mathbf{Q}, \omega, z_1, z_1)$ is equal to the surface electrical field propagator (Eq. (27)) which is the solution of Dyson's equation (Eq. (25)) for $n = 3$, where the dynamical response of the topmost GR layer is passivised, i.e.

$$\sigma_{\alpha\beta}^{i=1}(\omega) = 0.$$

Finally, after solving matrix equation (Eq. (36)), the spectra of electromagnetic modes in $GNR/h\text{-BN/GR}$ nanostructures can be calculated from

the following relation,

$$S_{\mu\nu}^{\text{GNR}}(\mathbf{Q}, \omega) = -\text{Re}\{\mathcal{E}\}_{\mu\nu, \mathbf{g}=\mathbf{g}'=\mathbf{0}}^{\text{GNR}}(\mathbf{Q}, \omega, z_1, z_1). \quad (38)$$

This procedure can be applied without loss of generality to any number of background layers, $n > 3$.

Computational details

All calculations (in atomistic and in 2D models) consisted of three major steps:

1. the ab initio DFT calculation of the ground state crystal structure and electronic structure, i.e. obtaining the Kohn-Sham (KS) states,
2. the calculation of the RPA photon self-energy, i.e. the tensor of the nonlocal optical conductivity $\sigma_{\mu\nu, \mathbf{G}, \mathbf{G}'}(\mathbf{Q}, \omega)$,
3. solving Dyson's equation for the photon propagator, here referred to as the electrical field propagator \mathcal{E} .

Electronic Ground State. To obtain the crystal and electronic ground states of the studied systems, ab initio plane-wave density functional theory (DFT) calculations were performed in Quantum Espresso 6.4 code⁵⁹⁻⁶¹ using the vdW-DF-cx functional⁶². Core electrons on all atoms were treated in the pseudopotential scheme using the optimised norm-conserving Vanderbilt pseudopotentials (ONCVPSP) provided by PseudoDojo^{63,64} for all three atom types (C, B, N). We relaxed each structure self-consistently until forces on all atoms were below 1 mRy a_0^{-1} while keeping the cell parameters fixed to their experimental values obtained from the Materials Project⁶⁵. The obtained optimised distance between graphene and *h*-BN layers was $\Delta z = 3.2 \text{ \AA}$. The cell constant for GR was set to $a = 4.664 a_0$, and for *h*-BN to $a = 4.747 a_0$, while the perpendicular cell size was set to $c = 7a$ to ensure no interaction occurs between periodic replicas. GR/*h*-BN/GR trilayer cell parameters were strained to the graphene cell size. The Brillouin zone (BZ) was sampled with a $13 \times 13 \times 1$ Monkhorst-Pack mesh and wavefunction/charge density cutoffs were converged to 55/240 Ry for monolayer graphene, 80/320 Ry for monolayer *h*-BN and 65/280 Ry for the GR/*h*-BN/GR trilayer, respectively. The Methfessel-Paxton electron smearing parameter was kept at 10 mRy for all calculations. Band structure calculations were performed along the high-symmetry path ($\Gamma\text{K}\Gamma$) with a total of 150 equidistant \mathbf{k} -points. Thereafter, we projected the resulting bands onto atomic states; allowing for the determination of their σ and π character. Additionally, exact diagonalizations were performed for each \mathbf{k} -point on a much denser $201 \times 201 \times 1$ Monkhorst-Pack mesh, necessary for adequate spectral resolution in subsequent excited states calculations. Summations over bands were performed over 40 bands for GR, 60 bands for *h*-BN, and 100 bands for GR/*h*-BN/GR.

RPA Conductivity Tensor $\sigma_{\mu\nu}$. The RPA optical conductivities are calculated for four different doping concentrations a) 0 e cm⁻² b) 1×10^{13} e cm⁻² c) 5×10^{13} e cm⁻² and d) 1×10^{14} e cm⁻² per graphene layer, which corresponds to Fermi level shifts relative to the Dirac point of a) 0 meV, b) 306 meV c) 673 meV and d) 932 meV, respectively.

In the *atomistic model*, the trilayer ground state wavefunction was used to calculate the RPA current-current conductivity tensor (Eq. (11)), including local-field effects up to a cut-off of $E_{\text{cut}}^{\text{lf}} = 25 \text{ Ha}$ (corresponding to 65 G_z Fourier components) in the z direction. Here a large number of local-field vectors is essential to correctly describe induced electric fields and current fluctuations perpendicular to the heterostructure plane where the induced electric fields are expected to strongly vary along the z -axis. However, only the zeroth component ($\mathbf{G}_{\parallel} = \mathbf{G}'_{\parallel} = \mathbf{0}$) was taken into account in the xy direction. The latter is shown to be adequate in IR and visible frequency range when the wavelength of the induced electric field $\lambda = 2\pi c/\omega$ much larger than the unit cell parameter a ($\lambda \gg a$)^{14,38}. The relaxation processes within the system due to electron-impurity, electron-phonon and electron-electron scattering processes were accounted for phenomenologically in terms of the relaxation-time approximation

(RTA)^{66,67}, with separate intraband and interband damping parameters set to $\eta_{\text{intra}} = 10 \text{ meV}$, $\eta_{\text{inter}} = 50 \text{ meV}$, respectively. Finally, we solve Dyson's equation and obtain the screened current-current conductivity tensor for the trilayer (Eq. (14)). The spectra of surface electromagnetic modes are determined from the real part of the $\mathcal{E}(\mathbf{Q}, \omega)$ in the topmost graphene layer z_1 (Eq. (16)) which is essentially the z, z' integrated screened conductivity $\bar{\sigma} = \sigma/(1 - \Gamma\sigma)$ so it represents the absorption of monochromatic electromagnetic wave ($\mathbf{Q}, \beta_0, \omega$) throughout the entire heterostructure.

In the *2D model*, the ground state wavefunctions for GR and *h*-BN monolayers were first used to calculate their respective conductivity tensors $\sigma_{\mu\nu}^{\text{GR}}$ and $\sigma_{\mu\nu}^{\text{h-BN}}$ (according to Eq. (11)) for $\mathbf{G} = \mathbf{G}' = \mathbf{0}$ and thus obtaining the 2D local conductivities (Eq. (19)) for each layer. The intraband and interband and damping parameters were kept the same as in the atomistic model corresponding to $\eta_{\text{intra}} = 10 \text{ meV}$ and $\eta_{\text{inter}} = 50 \text{ meV}$, respectively. The separation between GR and *h*-BN sheets was set to $\Delta z = 3.2 \text{ \AA}$ matching the relaxed crystal structure. Also, the separation between graphene planes and dielectric surfaces was fixed to $\Delta z_s = 3.0 \text{ \AA}$. Here we assumed that the dielectric medium is a vacuum (i.e. $\epsilon_0 = 1$) and that the substrate is alumina (Al_2O_3), described by a macroscopic dielectric function

$$\epsilon_s(\omega) = 1/\epsilon_{\mathbf{G}=\mathbf{0}\mathbf{G}'=\mathbf{0}}^{-1}(\mathbf{q} \approx \mathbf{0}, \omega), \quad (39)$$

where the dielectric matrix is $\hat{\epsilon} = \hat{1} - \hat{V}\hat{\chi}^0$ and the irreducible polarizability χ^0 is

$$\chi_{\mathbf{G}\mathbf{G}'}^0(\mathbf{q}, \omega) = \frac{2}{\Omega} \sum_{\mathbf{k} \in \text{BZ}} \sum_{n, m} \frac{f_n(\mathbf{k}) - f_m(\mathbf{k} + \mathbf{q})}{\omega + i\eta + E_n(\mathbf{k}) - E_m(\mathbf{k} + \mathbf{q})} \rho_{n\mathbf{k}, m\mathbf{k} + \mathbf{q}}(\mathbf{G}) \rho_{n\mathbf{k}, m\mathbf{k} + \mathbf{q}}^*(\mathbf{G}'). \quad (40)$$

Here, \mathbf{k}, \mathbf{q} and \mathbf{G} are the 3D wave vector, the transfer wavevector and the reciprocal lattice vector, respectively; corresponding to the bulk Al_2O_3 crystal. The charge vertices are $\rho_{n\mathbf{k}, m\mathbf{k} + \mathbf{q}}(\mathbf{G}) = \langle \phi_{n\mathbf{k}} | e^{-i(\mathbf{q} + \mathbf{G})\mathbf{r}} | \phi_{m\mathbf{k} + \mathbf{q}} \rangle$ and the bare Coulomb interaction is $V_{\mathbf{G}\mathbf{G}'}(\mathbf{q}) = \frac{4\pi}{|\mathbf{q} + \mathbf{G}|^2} \delta_{\mathbf{G}\mathbf{G}'}$. The ground state electronic density of the bulk Al_2O_3 is calculated using $9 \times 9 \times 3$ K-mesh, the plane-wave cut-off energy is 50 Ry and the Bravais lattices are hexagonal (12 Al and 18 O atoms in the unit cell) with the lattice constants $a_{\text{Al}_2\text{O}_3} = 4.76 \text{ \AA}$ and $c_{\text{Al}_2\text{O}_3} = 12.99 \text{ \AA}$. The Al_2O_3 irreducible polarizability χ^0 is calculated using the $21 \times 21 \times 7k$ -point mesh and the band summations (n, m) are performed over 120 bands. The damping parameter is $\eta = 100 \text{ meV}$ and the temperature is $T = 10 \text{ meV}$. For the optically small wave vectors $\mathbf{q} \approx \mathbf{0}$ the crystal local field effects are negligible, i.e. the crystal local field effects cut-off energy is set to zero. The detailed results for ϵ_s using this approach are presented in ref. 47. Using this approach, $\text{Re}\epsilon_s$ is almost constant ($\text{Re}[\epsilon_s] \approx 3$) for low frequencies ($\omega < 3 \text{ eV}$), i.e. in the IR and VIS range, while $\text{Im}\epsilon_s$ is equal to zero up to the band-gap energy ($E_g \sim 6 \text{ eV}$). Therefore, Al_2O_3 is a good choice for the substrate in the IR and visible frequency range since its electronic excitations are above that range which means that in the frequency range of interest, there is no dissipation of the electromagnetic energy in the substrate (it is transparent). Additionally, we explore the IR and VIS DP and AP which are above the Al_2O_3 IR active SO phonons (at $\omega_{\text{SO}} < 100 \text{ meV}$)⁶⁸ so that their hybridisation is negligible. Furthermore, the dielectric function is mostly constant, nevertheless, in this calculation, we used the fully dynamical and complex $\epsilon_s(\omega)$.

Subsequently, the electromagnetic energy absorption spectra are obtained from Eq. (16) after solving Dyson's equation (Eq. (25)) with the obtained spatially-resolved sum of local 2D conductivities (Eq. (24)) as described in detail in "Theoretical Formulation".

In order to excite the plasmon polaritons in the frequency range $\omega < 1 \text{ eV}$, the wavelength of the incident electromagnetic field should be in the range $\lambda_{\text{ph}} > 1200 \text{ nm}$ (IR/VIS spectrum). To make the electromagnetic field scattering more efficient, in the *GNR 2D model* we define a GNR grating of sub-wavelength width $d = 100 \text{ nm}$ and a period of $l = 2d = 200 \text{ nm} < \lambda$. Conversely, a SPP of wavelength $\lambda_{\text{SPP}} \sim l = 200 \text{ nm}$ is typically in the IR region $\omega_{\text{SPP}} \sim 100 \text{ meV}$, while the same IR photons have a wavelength of $\lambda_{\text{ph}} \sim 10000 \text{ nm}$. Therefore, the grating l enables the single-scattering of SPP

into the radiative region $Q = 1/\lambda_{\text{ph}} \approx 0$. All other parameters are the same as in the 2D model as described above.

By setting $\mathbf{Q} = Q_y \hat{y}$ we choose the p(TM) polarisation because we are interested in how the longitudinal p(TE) plasmon polariton converts into radiative resonances. We then proceed to compute the real part of the p(TM) electromagnetic field propagator from Eq. (36) and take its $\mathbf{g} = \mathbf{g}' = \mathbf{0}$ component, i.e. $\mathcal{E}_{yy, \mathbf{g}=\mathbf{g}'=\mathbf{0}}^{\text{GNR}}(Q_y \hat{y}, \omega, z_1, z_1)$. However, in order to classify more easily the eigenmodes that appear in the GNR, the calculation of the excitation spectrum is slightly modified, so that instead of the field (Eq. (38)), we rather calculate the induced current $\text{Re}[\sigma_{yy, \mathbf{g}=\mathbf{g}'=\mathbf{0}}^{\text{GNR}}(\omega) \mathcal{E}_{yy, \mathbf{g}=\mathbf{g}'=\mathbf{0}}^{\text{GNR}}(Q_y \hat{y}, \omega, z_1, z_1)]$, which essentially corresponds to the measurable absorption spectrum. The macroscopic field criteria $\mathbf{g} = \mathbf{g}' = \mathbf{0}$ means that we neglect the spatial resolution of the electromagnetic field within the unit cell l , i.e. in the limit $Q_y = 0$, the only dipolar (optically active) modes (the constant electrical field produced by a homogeneous distribution of the dipole momentum) will appear in the spectrum. However, by increasing Q_y , the multipolar GNR modes and their dispersion relations appear in the spectrum.

Data availability

The data generated and analysed supporting the findings of this work are available from the corresponding author upon reasonable request.

Code availability

The underlying code for this study is not publicly available but may be made available to qualified researchers on reasonable request from the corresponding author.

Received: 25 October 2023; Accepted: 31 March 2024;

Published online: 24 May 2024

References

- Low, T. et al. Polaritons in layered two-dimensional materials. *Nat. Mater.* **16**, 182–194 (2017).
- García de Abajo, F. J. Graphene plasmonics: challenges and opportunities. *ACS Photonics* **1**, 135–152 (2014).
- Barnes, W. L., Dereux, A. & Ebbesen, T. W. Surface plasmon subwavelength optics. *Nature* **424**, 824–830 (2003).
- Yan, H. et al. Damping pathways of mid-infrared plasmons in graphene nanostructures. *Nat. Photonics* **7**, 394–399 (2013).
- Bonaccorso, F., Sun, Z., Hasan, T. & Ferrari, A. C. Graphene photonics and optoelectronics. *Nat. Photonics* **4**, 611–622 (2010).
- Thygesen, K. S. Calculating excitons, plasmons, and quasiparticles in 2d materials and van der waals heterostructures. *2D Mater.* **4**, 022004 (2017).
- Basov, D., Averitt, R. & Hsieh, D. Towards properties on demand in quantum materials. *Nat. Mater.* **16**, 1077–1088 (2017).
- Basov, D. N., Fogler, M. M. & de Abajo, F. J. G. Polaritons in van der waals materials. *Science* **354**, aag1992 (2016).
- Ni, G. et al. Fundamental limits to graphene plasmonics. *Nature* **557**, 530–533 (2018).
- Liu, J.-P. et al. Graphene-based long-range spp hybrid waveguide with ultra-long propagation length in mid-infrared range. *Opt. Express* **24**, 5376–5386 (2016).
- Khurgin, J. B. How to deal with the loss in plasmonics and metamaterials. *Nat. Nanotechnol.* **10**, 2–6 (2015).
- Principi, A. et al. Plasmon losses due to electron-phonon scattering: the case of graphene encapsulated in hexagonal boron nitride. *Phys. Rev. B* **90**, 165408 (2014).
- Woessner, A. et al. Highly confined low-loss plasmons in graphene–boron nitride heterostructures. *Nat. Mater.* **14**, 421–425 (2015).
- Novko, D., Šunjić, M. & Despoja, V. Optical absorption and conductivity in quasi-two-dimensional crystals from first principles: Application to graphene. *Phys. Rev. B* **93**, 125413 (2016).
- Xia, F., Wang, H., Xiao, D., Dubey, M. & Ramasubramaniam, A. Two-dimensional material nanophotonics. *Nat. Photonics* **8**, 899–907 (2014).
- Geim, A. K. & Grigorieva, I. V. Van der Waals heterostructures. *Nature* **499**, 419–425 (2013).
- Caldwell, J. D. et al. Photonics with hexagonal boron nitride. *Nat. Rev. Mater.* **4**, 552–567 (2019).
- Dean, C. R. et al. Boron nitride substrates for high-quality graphene electronics. *Nat. Nanotechnol.* **5**, 722–726 (2010).
- Wang, B., Zhang, X., Yuan, X. & Teng, J. Optical coupling of surface plasmons between graphene sheets. *Appl. Phys. Lett.* **100**, 131111 (2012).
- Davanço, M., Urzhumov, Y. & Shvets, G. The complex bloch bands of a 2d plasmonic crystal displaying isotropic negative refraction. *Opt. Express* **15**, 9681–9691 (2007).
- Liao, W., Huang, Y., Wang, H. & Zhang, H. Van der Waals heterostructures for optoelectronics: Progress and prospects. *Appl. Mater. Today* **16**, 435–455 (2019).
- Novoselov, K. S., Mishchenko, A., Carvalho, A. & Castro Neto, A. H. 2D materials and van der Waals heterostructures. *Science* **353**, aac9439 (2016).
- Calman, E. V. et al. Indirect excitons in van der Waals heterostructures at room temperature. *Nat. Commun.* **9**, 1–5 (2018).
- Kovtyukhova, N. I., Perea-López, N., Terrones, M. & Mallouk, T. E. Atomically thin layers of graphene and hexagonal boron nitride made by solvent exfoliation of their phosphoric acid intercalation compounds. *ACS Nano* **11**, 6746–6754 (2017).
- Gao, X. et al. Contaminant-free wafer-scale assembled h-bn/graphene van der waals heterostructures for graphene field-effect transistors. *ACS Appl. Nano Mater.* **4**, 5677–5684 (2021).
- Li, Y. et al. Synthesis, microstructure and thermal stability of graphene nanoplatelets coated by hexagonal boron nitride (h-bn). *Mater. Chem. Phys.* **221**, 477–482 (2019).
- Hu, C. et al. Direct imaging of interlayer-coupled symmetric and antisymmetric plasmon modes in graphene/hbn/graphene heterostructures. *Nanoscale* **13**, 14628–14635 (2021).
- Baringhaus, J. et al. Exceptional ballistic transport in epitaxial graphene nanoribbons. *Nature* **506**, 349–354 (2014).
- Liu, J., Wright, A. R., Zhang, C. & Ma, Z. Strong terahertz conductance of graphene nanoribbons under a magnetic field. *Appl. Phys. Lett.* **93**, 041106 (2008).
- Ju, L. et al. Graphene plasmonics for tunable terahertz metamaterials. *Nat. Nanotechnol.* **6**, 630–634 (2011).
- Castro Neto, A. H., Guinea, F., Peres, N. M. R., Novoselov, K. S. & Geim, A. K. The electronic properties of graphene. *Rev. Mod. Phys.* **81**, 109–162 (2009).
- Wu, Z. et al. Graphene nanoribbon gap waveguides for dispersionless and low-loss propagation with deep-subwavelength confinement. *Nanomaterials* **11**, 1302 (2021).
- Zhao, W. et al. Nanoimaging of low-loss plasmonic waveguide modes in a graphene nanoribbon. *Nano Lett.* **21**, 3106–3111 (2021).
- Li, J., Zhu, L. & Arbogast, T. A new time-domain finite element method for simulating surface plasmon polaritons on graphene sheets. *Comput. Math. Appl.* **142**, 268–282 (2023).
- Yang, W., Li, J. & Huang, Y. Time-domain finite element method and analysis for modeling of surface plasmon polaritons. *Comput. Methods Appl. Mech. Eng.* **372**, 113349 (2020).
- Maier, M., Margetis, D. & Luskun, M. Dipole excitation of surface plasmon on a conducting sheet: finite element approximation and validation. *J. Comput. Phys.* **339**, 126–145 (2017).
- Andersen, K., Latini, S. & Thygesen, K. S. Dielectric genome of van der waals heterostructures. *Nano Lett.* **15**, 4616–4621 (2015).
- Despoja, V., Šunjić, M. & Marušić, L. Propagators and spectra of surface polaritons in metallic slabs: Effects of quantum-mechanical nonlocality. *Phys. Rev. B* **80**, 075410 (2009).

39. Li, P. et al. Infrared hyperbolic metasurface based on nanostructured van der Waals materials. *Science* **359**, 892–896 (2018).
40. Li, N. et al. Direct observation of highly confined phonon polaritons in suspended monolayer hexagonal boron nitride. *Nat. Mater.* **20**, 43–48 (2021).
41. Dai, S. et al. Graphene on hexagonal boron nitride as a tunable hyperbolic metamaterial. *Nat. Nanotechnol.* **10**, 682–686 (2015).
42. Giles, A. J. et al. Ultralow-loss polaritons in isotopically pure boron nitride. *Nat. Mater.* **17**, 134–139 (2018).
43. Pitarke, J. M. et al. Theory of acoustic surface plasmons. *Phys. Rev. B* **70**, 1–12 (2004).
44. Despoja, V., Djordjević, T., Karbunar, L., Radović, I. & Mišković, Z. L. Ab initio study of the electron energy loss function in a graphene-sapphire-graphene composite system. *Phys. Rev. B* **96**, 1–17 (2017).
45. Fei, Z. et al. Edge and Surface Plasmons in Graphene Nanoribbons. *Nano Lett.* **15**, 8271–8276 (2015).
46. Emani, N. K. et al. Plasmon resonance in multilayer graphene nanoribbons. *Laser and Photonics Rev.* **9**, 650–655 (2015).
47. Jakovac, J., Marušić, L., Andrade-Guevara, D., Chacón-Torres, J. C. & Despoja, V. Infra-red active Dirac plasmon series in potassium doped-graphene (Kc8) nanoribbons array on A_2O_3 substrate. *Materials* **14**, 1–17 (2021).
48. Zhao, B. & Zhang, Z. M. Strong plasmonic coupling between graphene ribbon array and metal gratings. *ACS Photonics* **2**, 1611–1618 (2015).
49. Jacob, Z., Alekseyev, L. V. & Narimanov, E. Optical hyperlens: far-field imaging beyond the diffraction limit. *Opt. Express* **14**, 8247–8256 (2006).
50. Britnell, L. et al. Strong light-matter interactions thin films. *Science* **340**, 1311–1315 (2013).
51. Baugher, B. W., Churchill, H. O., Yang, Y. & Jarillo-Herrero, P. Optoelectronic devices based on electrically tunable p-n diodes in a monolayer dichalcogenide. *Nat. Nanotechnol.* **9**, 262–267 (2014).
52. Koppens, F. H. et al. Photodetectors based on graphene, other two-dimensional materials and hybrid systems. *Nat. Nanotechnol.* **9**, 780–793 (2014).
53. Lee, C. H. et al. Atomically thin p-n junctions with van der Waals heterointerfaces. *Nat. Nanotechnol.* **9**, 676–681 (2014).
54. Wang, J., Mu, X., Sun, M. & Mu, T. Optoelectronic properties and applications of graphene-based hybrid nanomaterials and van der Waals heterostructures. *Appl. Mater. Today* **16**, 1–20 (2019).
55. Castilla, S. et al. Plasmonic antenna coupling to hyperbolic phonon-polaritons for sensitive and fast mid-infrared photodetection with graphene. *Nat. Commun.* **11**, 4872 (2020).
56. Tomaš, M. Green function for multilayers: light scattering in planar cavities. *Phys. Rev. A* **51**, 2545 (1995).
57. Novko, D., Lyon, K., Mowbray, D. J. & Despoja, V. Ab initio study of electromagnetic modes in two-dimensional semiconductors: application to doped phosphorene. *Phys. Rev. B* **104**, 115421 (2021).
58. Golenić, N. & Despoja, V. Trapped photons: transverse plasmons in layered semiconducting heterostructures. *Phys. Rev. B* **108**, L121402 (2023).
59. Giannozzi, P. et al. Quantum espresso: a modular and open-source software project for quantum simulations of materials. *J. Phys. Condens. Matter* **21**, 395502 (19pp) (2009).
60. Giannozzi, P. et al. Advanced capabilities for materials modelling with quantum espresso. *J. Phys. Condens. Matter* **29**, 465901 (2017).
61. Giannozzi, P. et al. Quantum espresso toward the exascale. *J. Chem. Phys.* **152**, 154105 (2020).
62. Berland, K. & Hyldgaard, P. Exchange functional that tests the robustness of the plasmon description of the van der Waals density functional. *Phys. Rev. B* **89**, 035412 (2014).
63. van Setten, M. J. et al. The PseudoDojo: training and grading a 85 element optimized norm-conserving pseudopotential table. *Comput. Phys. Commun.* **226**, 39–54 (2018).
64. Hamann, D. R. Optimized norm-conserving Vanderbilt pseudopotentials. *Phys. Rev. B* **88**, 085117 (2013).
65. Jain, A. et al. Commentary: The Materials Project: A materials genome approach to accelerating materials innovation. *APL Mater.* **1**, 011002 (2013).
66. Jablan, M., Buljan, H. & Soljačić, M. Plasmonics in graphene at infrared frequencies. *Phys. Rev. B* **80**, 245435 (2009).
67. Kupčić, I. Damping effects in doped graphene: the relaxation-time approximation. *Phys. Rev. B* **90**, 205426 (2014).
68. Ong, Z.-Y. & Fischetti, M. V. Theory of interfacial plasmon-phonon scattering in supported graphene. *Phys. Rev. B* **86**, 165422 (2012).

Acknowledgements

The authors acknowledge the financial support from QuantiXLie Center of Excellence, a project co-financed by the Croatian Government and European Union through the European Regional Development Fund – the Competitiveness and Cohesion Operational Program (Grant No. KK.01.1.1.01.0004). V.D. acknowledges the financial support from Croatian Science Foundation (Grant No. IP-2020-02-5556). S.d.G. acknowledges the support from the European Commission through the MAX Centre of Excellence for supercomputing applications (grant number 10109337 and 824143) and by the Italian MUR, through the Italian National Centre for HPC, Big Data, and Quantum Computing (Grant No. CN00000013). Computational resources were provided by CINECA.

Author contributions

N.G. performed all calculations, analysed and interpreted the results and wrote the manuscript. V.D. and S.d.G. proposed the topic of investigation and advised the scientific research. All authors discussed the results and contributed to the final manuscript.

Competing interests

The authors declare no competing interests.

Additional information

Correspondence and requests for materials should be addressed to Neven Golenić.

Reprints and permissions information is available at <http://www.nature.com/reprints>

Publisher's note Springer Nature remains neutral with regard to jurisdictional claims in published maps and institutional affiliations.

Open Access This article is licensed under a Creative Commons Attribution 4.0 International License, which permits use, sharing, adaptation, distribution and reproduction in any medium or format, as long as you give appropriate credit to the original author(s) and the source, provide a link to the Creative Commons licence, and indicate if changes were made. The images or other third party material in this article are included in the article's Creative Commons licence, unless indicated otherwise in a credit line to the material. If material is not included in the article's Creative Commons licence and your intended use is not permitted by statutory regulation or exceeds the permitted use, you will need to obtain permission directly from the copyright holder. To view a copy of this licence, visit <http://creativecommons.org/licenses/by/4.0/>.

© The Author(s) 2024